Zoisite in cratonic eclogite xenoliths - Implications for water in the upper mantle

I. B. Radu, Bertrand Moine, Nathalie Bolfan-Casanova, D. A. Ionov, Jean-Luc Devidal, E. Deloule, A. V. Korsakov, A. V. Golovin, O. B. Oleinikov, J. Y. Cottin

LITHOS 418-419 (2022) 106681

Contents lists available at ScienceDirect

LITHOS

journal homepage: www.elsevier.com/locate/lithos

Zoisite in cratonic eclogite xenoliths - Implications for water in the upper mantle

I.B. Radu [a,b,c,*], B.N. Moine [b], N. Bolfan-Casanova [d], D.A. Ionov [e], J.L. Devidal [d], E. Deloule [f], A.V. Korsakov [g], A.V. Golovin [g], O.B. Oleinikov [h], J.Y. Cottin [b]

[a] Department of Geosciences, Swedish Museum of Natural History, SE-104 05 Stockholm, Sweden
[b] Université de Lyon, UJM-Saint-Etienne, UCA, IRD, CNRS, Laboratoire Magmas et Volcans UMR6524, Saint-Etienne, France
[c] Department of Geological Sciences, 13 University Avenue, University of Cape Town, Rondebosch 7701, South Africa
[d] Laboratoire Magmas et Volcans, Université Clermont-Auvergne, CNRS UMR 6524, IRD R 163 Clermont-Ferrand, France
[e] GM., Université de Montpellier, Université des Antilles, Montpellier 34095, France
[f] CRPG, UMR7358, CNRS, Université de Lorraine, Vandoeuvre-lès-Nancy, France
[g] Sobolev Institute of Geology and Mineralogy, Siberian Branch Russian Academy of Sciences (SB RAS), Koptyuga 3, Novosibirsk 630090, Russian Federation
[h] Diamond and Precious Metal Geology Institute, SB RAS, Yakutsk 677007, Russian Federation

ARTICLE INFO

Keywords:
Eclogite xenoliths
Zoisite
Exsolution
Omphacite
Water
Nominally anhydrous minerals NAMs

ABSTRACT

A significant portion of the Earth's water is found at trace levels in nominally anhydrous rock forming minerals in the crust and mantle. Its distribution has far-reaching implications in melt-generating processes, mantle rheology and the stability of the lithosphere. We report petrographic, major and trace element, Fourier transform infrared spectroscopy and secondary ion mass spectrometry data on four eclogite xenoliths from the Obnazhennaya kimberlite, Siberia that contain hydrous minerals at upper mantle conditions. Al-rich (>9.9 wt% Al_2O_3) omphacitic clinopyroxene, a major mineral of eclogites, contains crystallographically controlled exsolutions of CaO-rich (up to 23.6 wt%) garnet (coronae, lenses), garnet-zoisite (lamellae) or amphiboles (needle/blade-like exsolutions). The omphacite hosting the exsolved lamellae shows enrichment or depletion in major (Al, Si, Mg) and trace (e.g., HREE) elements compatible with garnet and zoisite, proportional to the abundance of exsolutions.

We argue that zoisite likely formed concomitantly with garnet exsolution from a water- and Al-rich precursory omphacite, without any fluid addition. The compositional gradients are consistent with diffusion-controlled partitioning in a closed system, and their preservation indicates the exsolution likely took place shortly prior to eclogite entrapment by the kimberlite. Large, non-exsolved, omphacite grains contain minimum ~870–1500 ppm wt. H_2O (determined as OH). We infer that intertwined lamellae of hydrous garnet (600–960 ppm wt. H_2O) and minor (<1%) zoisite (2 wt% H_2O) formed at mantle conditions due to progressive exsolution, without external fluids. Recalculated whole rock water contents range from ~320 to 970 ppm wt. H_2O. These estimates exceed by far those for the surrounding peridotitic mantle and suggest that, although a minor component, eclogites may locally be an important water reservoir in the cratonic mantle.

1. Introduction

Water has been of major importance throughout Earth's history, from influencing the planet's early evolution to the present-day tectonics and up to the development of life (Peslier, 2010). Water (term used hereafter to refer to H_2, OH^- and/or H_2O species) preserved in trace amounts in the structure of nominally anhydrous minerals (NAMs) was shown to have an important influence on their physical and chemical properties (Demouchy and Bolfan-Casanova, 2016; Kolesnichenko et al., 2018). Water stored in structural defects in upper mantle NAMs is thought to trigger localized melts in the asthenosphere by decreasing the melting temperature of peridotite (Green et al. (2010)), to decrease the mechanical strength of minerals and favour deformation (Mei and Kohlstedt, 2000), properties that govern volcanism, earthquakes and crustal destabilization (Li et al., 2008; Libowitzky and Beran, 2006).

* Corresponding author at: Department of Geosciences, Swedish Museum of Natural History, SE-104 05 Stockholm, Sweden.
E-mail address: ioanabogdana.radu@gmail.com (I.B. Radu).

https://doi.org/10.1016/j.lithos.2022.106681
Received 15 June 2021; Received in revised form 28 February 2022; Accepted 19 March 2022
Available online 24 March 2022

Water distribution on Earth is dominated by crust-mantle interactions. Mantle outgassing through volcanic activity releases water (Jaffres et al., 2007), while subduction re-introduces water into the mantle by crustal recycling (Demouchy and Bolfan-Casanova, 2016; Ohtani et al., 2018; Peslier et al., 2002). Zoisite ($Ca_2Al_3Si_3O_{12}(OH)$) is an important hydrous phase in the subducted oceanic crust and may significantly contribute to the fluid budget in the mantle beyond the amphibole stability field (100–120 km depth) (Feineman et al., 2007; Poli and Schmidt, 1995). Due to its high-water content (2 wt%), high-pressure stability and relatively high density of 3.35 g/cm^3, zoisite has the potential to transport water into the upper mantle (Maruyama and Okamoto, 2007; Poli and Schmidt, 1998). High-pressure and temperature experiments constraining phase relation diagrams in the simplified CASH (CaO-Al_2O_3-SiO_2-H_2O) system demonstrate the stability of zoisite up to ~6–7 GPa, above 900 °C (Poli (2016) and references therein). A number of previous studies focused on zoisite as the by-product of fluid-assisted retrogression (Massonne, 2012), and a single study described it in a clinopyroxenite xenolith from the lower crust (Xu et al., 2004). In this study we evaluate if zoisite could form in eclogite within the lithospheric mantle.

Eclogite xenoliths sampled by kimberlites are interpreted as the oldest remnants of recycled oceanic crust preserved in the cratonic lithospheric mantle (Radu et al. (2019) and references therein). Omphacitic clinopyroxene, a major mineral of eclogites, may contain up to thousands of ppm of water and is thus the NAM with the highest water content in the upper mantle (Bell and Rossman, 1992; Li et al., 2008; Peslier, 2010; Skogby, 2006). Due to the slow solid-state diffusion of structurally bound water in clinopyroxene (Demouchy et al., 2011; Ingrin and Skogby, 2000), mantle clinopyroxenes are believed to largely preserve the water they had originally (Sundvall and Stalder, 2011) and may account for most of the upper mantle water budget (Kovacs et al., 2016). However, non-metasomatized eclogite xenoliths hosting well-preserved, inclusion-free omphacites are rare (Huang et al., 2014), and estimates of their water content are scarce and poorly constrained.

In this study we report non-metasomatised, large omphacite crystals hosting crystallographically-controlled (topotactic) exsolutions of garnet±zoisite lamellae and amphibole needles/blades, as well as homogeneous, non-exsolved omphacite grains from four non-metasomatized eclogites from Obnazhennaya kimberlite (Siberia). We assess the stability of hydrous exsolutions at mantle conditions in an isochemical system and quantify the amount of water that can be stored in mantle eclogites, in particular in omphacite. Lastly, we attempt to retrace the origin of the water stored in mantle eclogites, in the context of their petrogenesis as recycled oceanic crust.

2. Geological background

The Siberian craton (Fig. 1) occupies most of the Republic of Yakutia in the Russian Federation and is the largest (~4 million km^2) Archaean to Palaeoproterozoic domain on Earth. It is delimited in the north and east by Taimyr and Verkhoyansk sedimentary fold belts, and in the west and south by the Central-Asian and Mongol-Okhotsk volcanic orogenic belts, respectively (Rosen et al., 2005). The craton comprises several terranes ranging roughly in age from 3.6 to 2.3 Ga (Pisarevsky et al., 2008) amalgamated by 2.2–1.9 Ga (Rosen et al., 2005). Three main intervals of kimberlite magmatism on the Siberian craton took place at 367–345 Ma, 245–215 Ma and 160–145 Ma (Alifirova et al., 2012; Griffin et al., 1999).

Obnazhennaya pipe (70°15′ N–121°35′ E) is a group I kimberlite, located near the NE border of the craton and part of the Kuoyka kimberlite field in the Olenek province (Ionov et al., 2018). The Obnazhennaya eruption age is poorly constrained (Late-Jurassic to Early Cretaceous). Rb—Sr data in phlogopite phenocrysts from the Kuoyka field yield 157 ± 2 Ma (Agashev et al., 2004) and paleomagnetic age determination indicate 168 ± 11 Ma (Blanco et al., 2013). However, most authors agree on an age estimate around ~160 Ma placing it in the

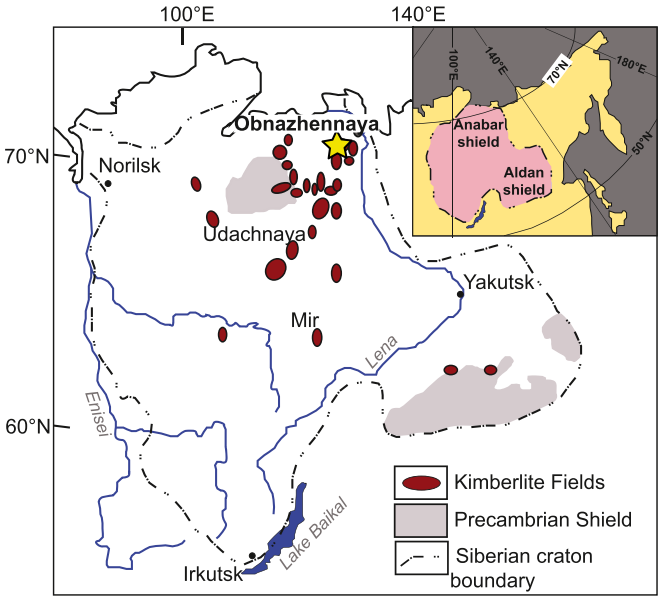

Fig. 1. Map of the Siberian craton with outcropping Precambrian shields and main kimberlite pipes. Obnazhennaya kimberlite is marked with a yellow star symbol. After Taylor et al. (2003). (For interpretation of the references to colour in this figure legend, the reader is referred to the web version of this article.)

youngest kimberlite magmatic event. The xenolith suite comprises xenocrysts, coarse-grained peridotite, eclogite, websterite and dunite mantle fragments (Taylor et al., 2003). Petrographic and geochemical data, the absence of sheared mantle lithologies and xenoliths equilibrated at high pressure conditions suggest a thin lithospheric mantle (≤100 km) beneath Obnazhennaya (Ionov et al., 2019).

3. Analytical methods

Mineral major element analyses were performed with a Cameca SX-100 electron microprobe at the Laboratoire Magmas et Volcans, Université Clermont Auvergne, France and with a JEOL JXA-8320 electron microprobe at the Geology Department, Rhodes University, South Africa. Operating conditions were 15-kV and a sample current of 15-nA. The counting time was 10 s for background and 20 s for all elements, except for K and Na – 60s under specific setting (low current intensity and background after peak measurement to limit alkali volatilisation) to ensure high precision for K in omphacite and Na in garnet. All data was processed using full ZAF Cameca PAP corrections. The distribution maps were carried out using 15 keV accelerating voltage and 20 nA current, at 14 × 14 μm (XY) intervals, 1100 × 1750 points and the quantitative profiles at 1 μm steps, 2200 points.

Mineral trace element compositions were acquired by LA-ICP-MS at the Laboratoire Magmas et Volcans, Université Clermont Auvergne, France, using a Agilent 7500cs ICP-MS associated to a Resonetics M-50 laser powered by an ultra-short pulse ATL Excimer Ar/F laser system operating at 193 nm. Beam diameter was set at 100 μm, with a 6–8 Hz repetition rate and 2.8 J/cm^2 fluency (detailed description in Müller et al. (2009)). NIST612 reference glass was used for instrument tuning and as primary standard to calculate concentration; ^{44}Ca measured in analogue mode was used as internal standard and for each session BCR-2 g was used as secondary standard. Data reduction was carried out with the software package GLITTER® (Macquarie Research Ltd., 2001)(van Achterbergh et al., 2001). The time resolved signal for each element was carefully monitored to discard perturbations related to inclusions, fractures or mixing for each analysis. The analyses reproducibility and accuracy were estimated through repeated analyses of BCR-2G USGS standard at the beginning and at the end of every sequence. Accuracy better than 10% is obtained.

Mineral modes were determined on thin section scans and compositional maps (~10–20% uncertainty due to variable grain size and distribution), using the Adobe®Photoshop® image-editing software. Quantification was based on colour contrast between the different phases, with negligible errors in surface to volumetric conversions (~5 %) due to similar densities of the specific minerals. No preferred orientation of grains or layering in the rock is observed. Reconstructed precursory omphacite and whole rock compositions were calculated based on individual mineral analyses and estimated mineral modes.

Sample preparation for Infrared spectroscopy was done by hand-picking individual omphacite and garnet crystals under a binocular microscope. Between 2 and 3 omphacite crystals were selected from each of the four samples, and with the use of cleavage features and extinction under the optical microscope, the crystallographic c axis was identified. These crystals were oriented parallel to the (100) and (010) faces, corresponding to the directions of the main refractive indices (α, β and γ) (see detailed procedure in Stalder and Ludwig (2007)). Crystal thickness varies between 240 and 570 μm for both (100) and (010) orientations. These grains were analysed before and after being heated in air, at 500°C, for 12h. Additionally, between 10 and 22 omphacite crystals of random crystallographic orientation were double polished and thinned to 450–600 μm for unpolarised analyses. Polarised FTIR spectra were acquired in the 700–7500 cm^{-1} range, along the directions of the main refractive indices, with a Bruker Vertex 70 spectrometer coupled with a Hyperion 3000 microscope at the Swedish Museum of Natural History, Stockholm. For each analysis, 250 scans were collected and averaged, with same number of scans for background, using a spectral resolution of 4 cm^{-1}. Similarly, unpolarised FTIR spectra were acquired in the 700–7500 cm^{-1} range, on randomly oriented grains, with a Bruker Vertex 70 spectrometer coupled with a Hyperion microscope at the LMV, Cézeaux, France. For each analysis, 300 scans were collected and averaged, with 100 scans for background, using a spectral resolution of 2 cm^{-1} and an aperture size of 10 × 10 to 50 × 50 μm. Cracks and opaque areas were avoided by adapting the aperture size for masking during analysis. All obtained spectra were baseline corrected and the characteristic OH bands were fitted with the PeakFit software. The water contents were calculated through a modified equation of the Beer-Lambert law: $c = A_{tot}/(\varepsilon \times t)$, where c is the water content in ppm by weight, A_{tot} is the sum of the integrated absorbance measured parallel to the optical indicatrix directions (α, β, γ) expressed in cm^{-2}, t is the thickness in cm and ε is the specific absorption coefficient. In the case of unpolarised radiation a minimum of 10 absorbance measurements per sample is required for a ~20% estimated error and the resulting averaged total absorbance must be multiplied by three (Kovacs et al., 2008). As garnet is isotropic, no specific number of analyses was statistically required for the chosen calibration. Water contents calculated for omphacite using different absorption coefficients by Bell et al. (1995), Koch-Müller et al. (2007) and the wavenumber-dependent calibration by Libowitzky and Beran (2006) were compared. Water calculation in garnet was attempted with the pyrope absorption coefficient by Bell et al. (1995) and the hydrogrossular calibration of Rossman and Aines (1991).

Total hydrogen determinations and hydrogen profile were acquired with a Cameca IMS1280 HR ion microprobe at CRPG-CNRS Nancy, on a polished, gold-coated thin section. The analytical conditions for the O^- primary beam were 13 keV, ~10 nA, 30 μm diameter spot, and for the secondary beam mass resolution was set at 2000, with an energy window of 55 eV and no energy filtering. Secondary ions (for $^1H^+$, $^2H^+$, $^{28}Si^+$ and $^{30}Si^+$) were measured by peak switching with 20 min ion counting time. Count rates on H^+ varied between 1.105 and 2.105 counts/s and statistical precision ranged from 5x to 10x. The H^{2+}/H^+ ratio was always below 10^3, attesting to a minimal instrumental contribution. Water content of the background was inferior to 10 ppm. The hydrogen distribution profile was traced in the host omphacite, in-between two exsolved lamellae, with a step increase of 20 μm. Sample water content was calculated based on the measured secondary hydrogen ion intensity (the secondary $^1H^+$ counts with respect to the primary ion intensity ratio) of several measurements on the augite standard (NSH3–1300 ppm, Xia et al., 2004), as there is currently no omphacite SIMS standard, using a working curve of H^+/Si^+ vs. H_2O wt% values (1σ = 0.01 wt% H_2O). Experimental studies on silicate glasses evidence that matrix differences between the reference material and the samples due to distinct Na^+/Ca^{2+}, causes at most ~30% overestimate in water content, calculated based on H^+/Si^+ ratio (Deloule et al., 1995). More details about the analytical conditions and the calculated value are found in Moine et al. (2020).

4. Results

4.1. Petrography

Four centimetre-sized eclogite xenoliths (one bimineralic and three corundum-bearing) from the Obnazhennaya kimberlite were studied in

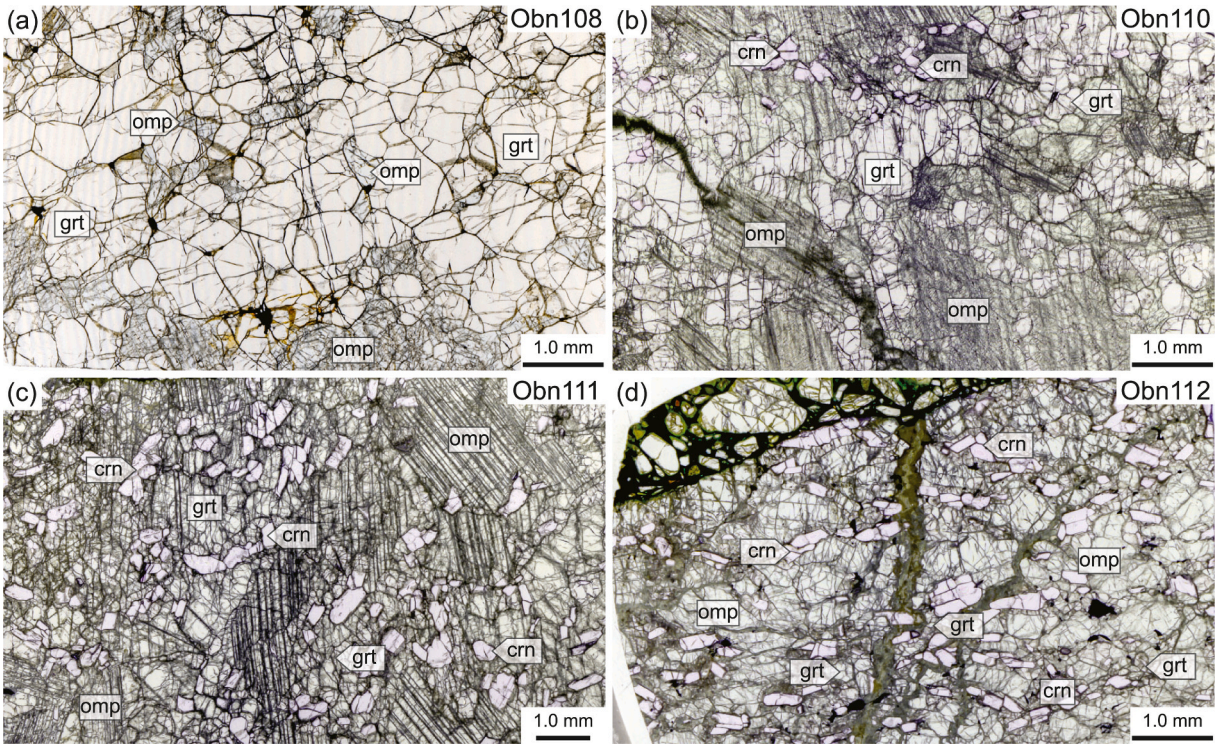

Fig. 2. Scanned thin sections of bimineralic (a) and corundum-bearing (b–d) eclogites from Obnazhennaya. Omphacite occurs as subhedral, light green, inequigranular large grains that exhibit cleavage planes marked by thin exsolutions. Garnet ranges from subhedral to rounded, with straight grain boundaries and of light brown colour. Corundum occurs as intense pink sub- to anhedral grains. (For interpretation of the references to colour in this figure legend, the reader is referred to the web version of this article.)

detail (summary of petrography in Appendix A). Their major primary mineral phases are garnet (grt) and omphacitic clinopyroxene (omp), occasionally including minor corundum (Fig. 2), with a broad range of grain size and modal abundances. All four samples have a fresh aspect (Supplementary Fig. 1) and show a sharp contact with the host kimberlite. The reaction rim is narrow (~200 μm) and is notably marked by white, opaque destabilized omphacite. The samples belong texturally to non-metasomatised eclogites (Gréau et al., 2011; MacGregor and Carter, 1970), showing none of the characteristics typical for kimberlite-derived metasomatism (i.e., serrated grain boundaries, dusty aspect due to fluid inclusions, keliphitic textures). Two samples have discordant veins intruding from the host kimberlite (Fig. 2b–d), however no minerals specific for kimberlitic/carbonatite metasomatism (e.g., phlogopite, spinel, carbonates, amphibole-plagioclase intergrowths) are found outside veinlets, suggesting limited interaction with the host magma.

Bimineralic eclogite Obn108 is dominated by light coloured garnet (~77 vol%), with straight grain boundaries (Fig. 2a). Garnet ranges from large (~0.7 mm), subhedral crystals, often surrounded by secondary rims of fine-grained, opaque material, to small (~0.2 mm), lens-shaped, exsolved grains (~15% relative modal abundance – rel. mod.). The latter occur as discontinuous, iso-oriented exsolutions in omphacite, developed along the cleavage planes. Omphacite occurs as anhedral, light green, crystals that commonly show strong cleavage planes. In addition to the lens-shaped garnet, omphacite also contains fine-grained needle/blade-like amphibole (<10 μm, Fig. 3a) exsolutions, oriented along one of the main cleavage directions, parallel to the garnet lenses. Where present, rutile occurs as interstitial, anhedral grains, associated with interstitial carbonate-rich veinlets. This texture corresponds to that described by Gréau et al. (2011) for non-metasomatized eclogite xenoliths.

In the corundum-bearing eclogites (Obn110, Obn111, Obn112), omphacite is the most abundant mineral (~60 vol%), ranging from small (~0.3 cm) rounded grains to large (~2 cm) subhedral light green crystals (Fig. 2 b–d). The large omphacite contains strongly distinct cleavage planes with oriented garnet (~5% rel. mod.) and garnet-zoisite lamellae (~10% rel. mod.) and is predominant. Additionally, garnet occurs as subhedral to subrounded grains, with straight grain boundaries and of typically light brown colour (Fig. 2b–d). Garnet mode decreases from sample Obn110 (40 vol%) to Obn112 (25 vol%), whereas corundum (crn) increases from ~4 to 17 vol%. Corundum occurs as subhedral to anhedral, pale to intense pink crystals, often surrounded by garnet coronae when in contact with omphacite. Rutile is scarce and commonly interstitial.

In summary, five types of microtextures occur in omphacite (Fig. 3): (i) fine needle/blade-like amphiboles (<10 μm), garnet ±zoisite as (ii) oriented lamellae, (iii) coronae, (iv) lenses and (v) granular clusters. The topotaxial lamellae (~50–300 μm) occur as two generations: initial garnet and intertwined garnet–zoisite developed along the omphacite cleavage planes (Fig. 3b–d), crosscut by another generation of garnet lamellae. Both generations extend along the length of the host crystal and have sharp boundaries. Zoisite (Supplementary Fig. 2) locally occurs as euhedral crystals (~10% rel. mod.) in garnet-zoisite lamellae, and the contact between zoisite and the exsolved garnet as well as the host omphacite is sharp, with no apparent breakdown (Fig. 3e–f). There

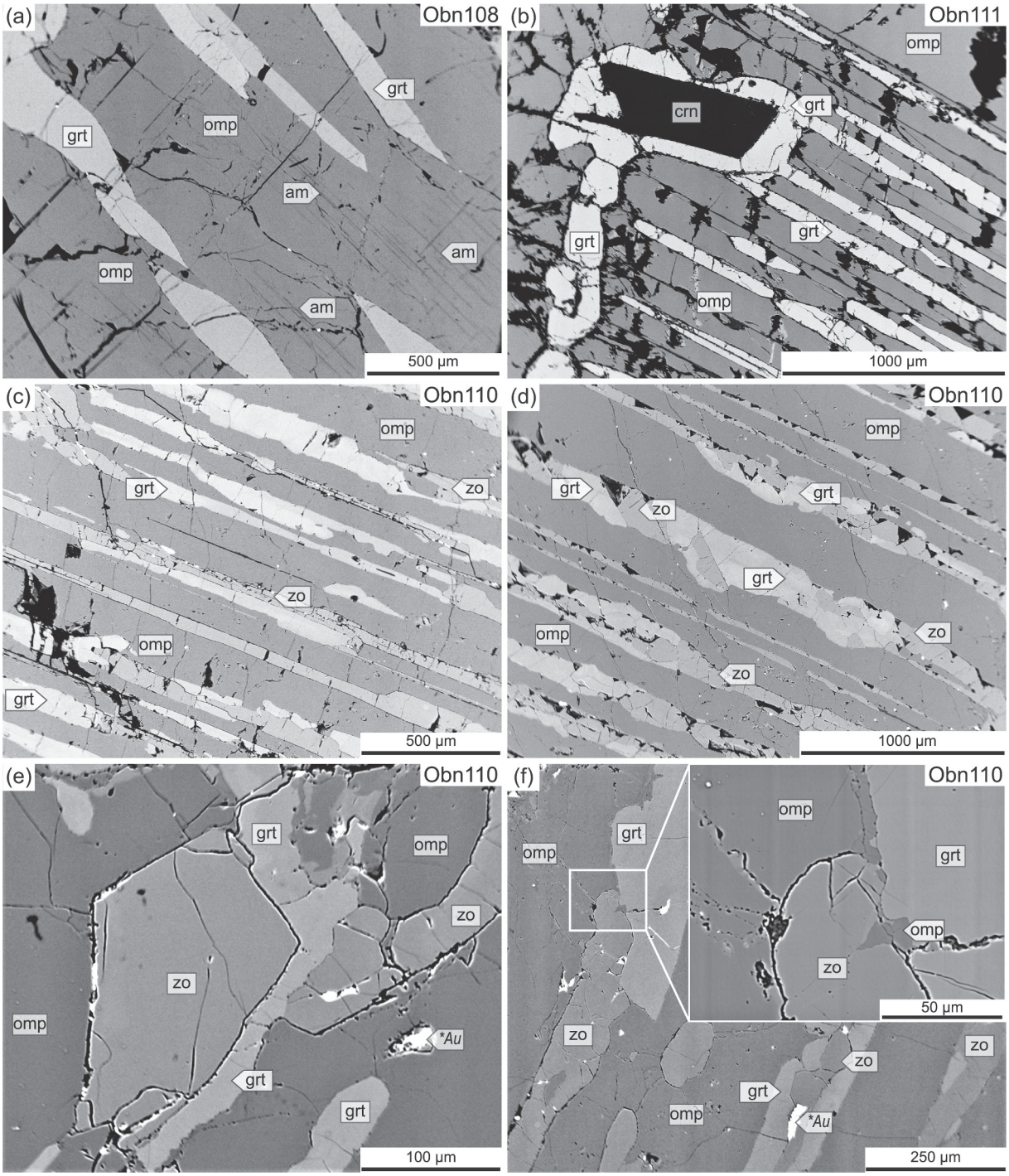

Fig. 3. BSE images of representative exsolution textures. Large omphacite grains exhibit topotaxial amphibole needles/blades (a), garnet (a–b) or garnet-zoisite (c–d) exsolution lenses and lamellae. Some samples contain crosscutting garnet lamellae in between the cleavage planes. Corundum grains are often surrounded by monophasic (garnet) coronae. Zoisite may occur as euhedral crystals (e) and exhibit sharp grain boundaries towards garnet and the host omphacite.

is a continuity between the lamellae and corona textures, with garnet lamellae blending into the coarse coronae (Fig. 3b). The latter are developed around corundum and are typically monophasic, consisting of garnet. Comparably, lens-shaped (~0.6 mm) and fine-grained (~0.1 mm) granular clusters ("necklace") garnet exsolutions are found aligned with the main omphacite cleavage planes (Fig. 3a), with the latter extending to follow the host omphacite grain boundaries. Similar garnet exsolution textures were previously described in eclogite xenoliths (e.g. Kaapvaal, (Harte and Gurney, 1975); Tanzanian,; Siberian, Jerde et al. (1993), Sun et al. (2020)).

4.2. Major element mineral chemistry and P-T estimates

Representative mineral major element compositions are provided in Table 1 and full results are given in Appendix B. All four samples have low Na_2O content in garnet (0.01–0.06 wt%) and low K_2O in clinopyroxene (0.01–0.07 wt%), consistent with them being pristine, unaffected by kimberlite metasomatism (Huang et al., 2012), (Gréau et al., 2011; Radu et al., 2017). Based on cation distribution on the M sites, all clinopyroxene have a jadeite content of 25–27% and the samples are eclogites sensu-stricto (Morimoto, 1988). The MgO content in

Table 1
Representative major element (wt%) and cation compositions for garnet, omphacite and zoisite in bimineralic and corundum-bearing eclogite xenoliths from the Obnazhennaya kimberlite.

Sample	Obn108				Obn110					Obn111				Obn112		
	garnet		omphacite		garnet		omphacite		zoisite	garnet	omphacite		zoisite	garnet	omphacite	
	p	e	p	e	p	e	p	e	e	e	p	e	e	e	p	e
SiO_2	41.18	40.62	50.19	52.17	41.53	40.88	49.06	52.19	38.92	40.06	49.14	51.90	39.15	40.00	50.48	50.79
TiO_2	0.09	0.05	0.18	0.31	0.09	0.02	0.11	0.05	0.04	0.04	0.01	0.07	0.02	0.06	0.05	0.05
Al_2O_3	23.56	23.17	14.74	10.61	23.66	23.58	19.37	14.84	33.65	23.14	18.66	14.84	32.74	22.71	16.02	15.61
Cr_2O_3	0.05	0.15	0.07	0.11	b.d.	0.04	0.07	0.08	0.05	0.07	0.02	0.03	b.d.	0.02	0.05	0.05
FeO_t	8.69	7.38	1.81	2.01	8.05	6.47	1.04	0.94	0.57	5.07	1.09	0.91	0.36	5.99	1.18	1.16
MnO	0.13	0.06	0.01	0.04	0.19	0.09	0.01	0.00	0.01	0.11	0.02	0.07	0.04	0.08	0.00	0.00
MgO	15.94	10.95	9.84	11.63	16.50	14.52	8.35	9.53	0.05	8.31	8.50	9.57	0.56	8.18	9.25	9.42
CaO	10.40	17.65	19.48	19.53	10.77	14.37	18.54	17.81	24.82	23.06	19.10	18.11	24.77	22.91	18.93	18.91
Na_2O	0.03	b.d.	3.73	3.53	0.02	b.d.	3.99	4.34	0.03	b.d.	3.68	4.40	0.03	b.d.	3.94	3.96
K_2O	b.d.	b.d.	0.02	0.01	b.d.	b.d.	b.d.	0.01	b.d.	b.d.	0.03	b.d.	b.d.	b.d.	0.01	b.d.
Total	100.1	100.0	100.1	99.95	100.8	100.0	100.6	99.79	98.14	99.86	100.2	99.90	97.67	99.95	99.91	99.95
Si	2.96	2.97	1.79	1.87	2.95	2.94	1.74	1.85	2.95	2.94	1.75	1.84	2.98	2.95	1.80	1.81
Ti	0.01	0.00	0.01	0.01	0.01	0.00	0.00	0.00	0.00	0.00	0.00	0.00	0.00	0.00	0.00	0.00
Al	1.99	1.99	0.62	0.45	1.98	2.00	0.81	0.62	3.01	2.00	0.78	0.62	2.94	1.97	0.67	0.66
Cr	0.00	0.01	0.00	0.00	–	0.00	0.00	0.00	0.00	0.00	0.00	0.00	0.00	0.00	0.00	0.00
Fe^{2+}	0.44	0.39	0.01	0.01	0.37	0.27	0.03	0.03	0.00	0.21	0.03	0.03	0.00	0.24	0.04	0.04
Fe^{3+}	0.08	0.06	0.05	0.05	0.11	0.12	–	–	0.03	0.10	0.00	0.00	0.02	0.13	0.00	0.00
Fe_{tot}	0.52	0.45	0.05	0.06	0.48	0.39	0.03	0.03	0.03	0.31	0.03	0.03	0.02	0.37	0.04	0.04
Mn	0.01	0.00	–	0.00	0.01	0.01	–	0.00	0.00	0.01	0.00	0.00	0.00	0.01	0.00	0.00
Mg	1.71	1.19	0.52	0.62	1.75	1.56	0.44	0.50	0.01	0.91	0.45	0.51	0.06	0.90	0.49	0.50
Ca	0.80	1.38	0.75	0.75	0.82	1.11	0.70	0.68	2.02	1.82	0.73	0.69	2.02	1.81	0.72	0.72
Na	–	–	0.26	0.25	–	–	0.27	0.30	0.00	–	0.25	0.30	0.00	–	0.27	0.27
K	–	–	0.00	–	–	–	–	0.00	–	–	0.00	0.00	–	–	0.00	0.00
Mg#	0.77	0.73	0.91	0.91	0.79	0.80	0.93	0.95	–	0.75	0.93	0.95	–	0.71	0.93	0.93

The cations for garnet are shown for 12 O per formula unit and for omphacite for 6 O per formula unit, calculated with PET for Mathematica.
Mg# is molar $Mg/(Mg + Fe_{tot})$.
b.d. bellow detection limit.
p - primary; e- exsolved.

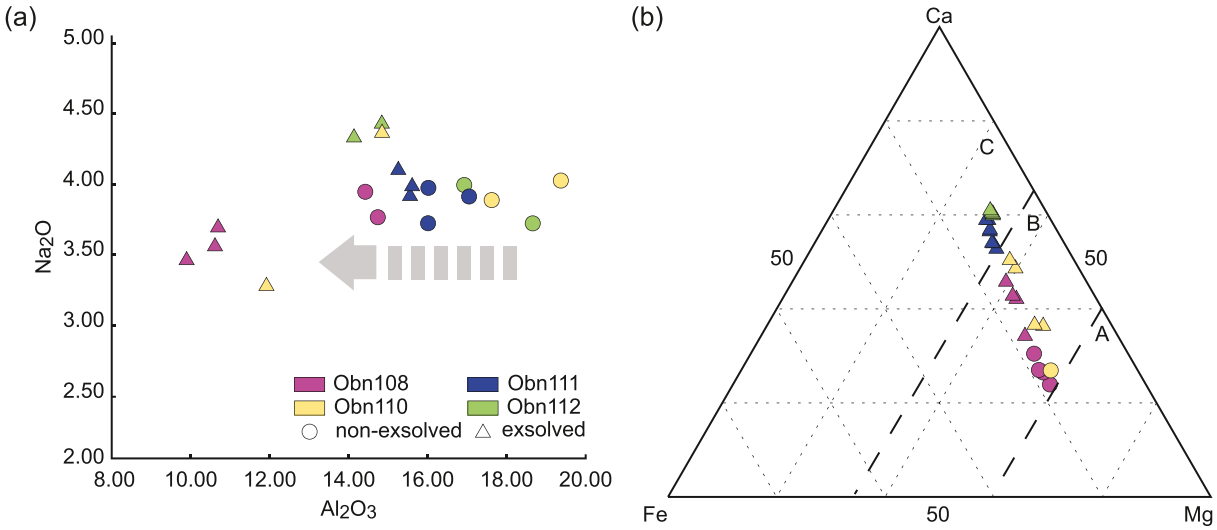

Fig. 4. Compositional diagrams of (a) Na_2O vs Al_2O_3 in omphacite showing a decrease in Al content with the degree of exsolution; and (b) main garnet endmembers showing an increase in Ca content from large to exsolved garnet. Non-exsolved grains are marked by circles, whereas exsolved grains (host omphacite or garnet exsolutions) are marked with triangles.

omphacite increases by ~2 wt% from the host to the exsolved grains, proportional to the amount of garnet ± zoisite expelled. By contrast, the Al_2O_3 content decreases with the degree of exsolution, from ~14.5 wt% to ~10.5 wt% and from 16.0–19.4 wt% to 11.9–16.0 wt%, in the bimineralic (Obn108) and in the corundum-bearing eclogites, respectively (Fig. 4a). The grossular and pyrope endmembers are dominant (Fig. 4b), with the Ca content significantly increasing from large grains (CaO ~10.6) to the exsolutions (CaO ~13.3–23.6). Composition profiles in the host clinopyroxene show a decrease in the Al content towards the exsolved garnet/garnet-zoisite lamellae, and a complementary increase in Si and Mg contents (Fig. 5). No variations in the Na, Ca and Fe contents are observed.

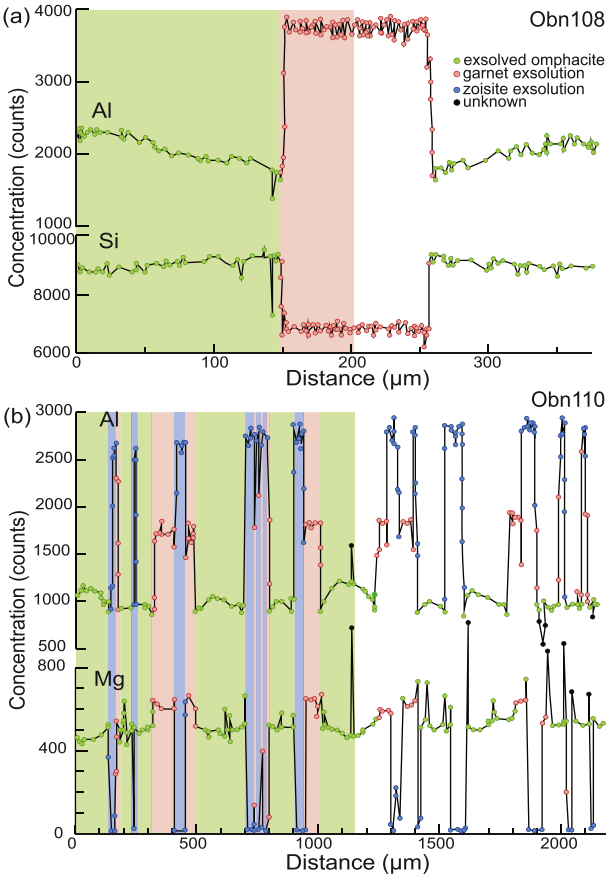

Fig. 5. Complementary diffusion gradients of Al, Si and Mg preserved in omphacite (green) hosting exsolved lamellae of (a) grossular-rich garnet (red) in sample Obn108 and (b) grossular-rich garnet (red) and zoisite (blue) in sample Obn110. (For interpretation of the references to colour in this figure legend, the reader is referred to the web version of this article.)

4.2.1. *P-T estimates*

Temperatures were calculated using several garnet-clinopyroxene thermo-barometers (Ellis and Green, 1979; Krogh, 1988; Krogh-Ravna, 2000; Nakamura, 2009) for 1 GPa, 3 GPa and 7 GPa. Pressures were then derived from the intercept between the temperature trend lines and the local conductive model geotherm (Pollack and Chapman, 1977) corresponding to a surface heat flow of 45 mW m^{-2} (estimated at 40 to >50 mW m^{-2}, Ionov et al. (2018)). For comparison, pressures were also calculated using the (Beyer et al., 2015) temperature-dependent geobarometer and the intercept with the 40 mW m^{-2} geotherm (estimated for Obnazhennaya websterites by Taylor et al. (2003)). All results are provided in Appendix C. The temperatures calculated with the (Krogh-Ravna, 2000) geothermometer coupled with the 45 mW m^{-2} geotherm yield equilibrium conditions of 850° – 1090°C and ~3–4 GPa, in good agreement with estimates by Sun et al. (2020) (Supplementary Fig. 3). In samples where temperatures were determined for both primary and exsolved omphacite-garnet pairs, the latter systematically yield higher temperatures, regardless of the chosen geothermometer. This is more likely due to the variable amount of Mg consumed during garnet growth, than a record of PT conditions during the exsolution.

Pressure and temperature estimates for mantle eclogites face numerous limitations, mostly imposed by their simple mineral assemblage. Moreover, in the case of samples exhibiting exsolutions, there is an obvious disparity between the results based on non-exsolved versus exsolved mineral pairs. In the latter case, the relevance and stability of equilibrium micro-domains is debatable. Therefore, the calculated values should be used with caution.

4.3. *Trace element mineral chemistry*

Representative trace element compositions of individual minerals are provided in Table 2 and full results are given in Appendix D. Extended element and REE patterns, normalized to the primitive mantle (McDonough and Sun, 1995), are shown in Fig. 6. Omphacite covers a range of profiles from LREE-rich (La/Sm_N ~4.41) patterns with strongly fractionated HREE (Sm/Yb_N ~167, bimineralic eclogite Obn108), to LREE-depleted ($La/Sm_N < 0.34$) and nearly flat to depleted HREE patterns (($Sm/Yb_N < 15$, corundum-bearing eclogites). The abundance of HREE in omphacite changes with the degree of exsolution. As the modal abundance of exsolved garnet and zoisite increases, the host omphacite becomes more depleted in elements such as HREE, Hf, Y which preferentially partition in the exsolved phases. Throughout the set of samples omphacite shows positive Eu (Eu* 1.41–2.95) and Sr (Sr* 3.02–33.6) anomalies.

Garnet patterns group similarly, into LREE-rich (Obn108, Fig. 6 a–b) and LREE-depleted (Obn110, Obn111, Obn112, Fig. 6 c–h). HREE can

Table 2
Representative trace element composition (ppm) of garnet, omphacite and zoisite in bimineralic and corundum-bearing eclogites from Obnazhennaya.

Sample	Obn108				Obn110					Obn111				Obn112			
	garnet		omphacite		garnet		omphacite		zoisite	garnet		omphacite		garnet		omphacite	
	p	e	p	e	p	e	p	e	e	p	e	p	e	p	e	p	e
Li	b.d.	b.d.	1.30	0.84	b.d.	0.40	4.63	5.25	31.5	b.d.	b.d.	b.d.	b.d.	0.46	0.09	5.81	4.35
Sc	30.4	4.49	3.00	0.81	47.2	14.2	3.48	1.66	1.13	57.7	14.7	6.09	2.54	46.1	12.2	3.96	7.33
Ti	770	394	1791	923	191	220	391	383	121	126	148	278	259	195	172	454	336
V	156	132	288	183	82.5	105	145	174	132	54.0	69.2	102	119	75.7	102	161	132
Cr	609	532	421	348	396	471	365	355	354	307	262	280	281	364	313	376	350
Co	135	50.5	21.8	11.7	125	74.6	24.8	23.7	0.84	95.4	46.6	22.3	22.9	48.7	27.4	14.8	17.5
Ni	65.9	43.1	426	301	137	86.1	841	866	15.6	91.1	54.3	742	866	21.3	15.0	253	193
Rb	b.d.	b.d.	b.d.	b.d.	b.d.	0.01	b.d.	b.d.	0.04	b.d.	0.01	b.d.	0.004	0.01	0.01	b.d.	b.d.
Sr	1.11	4.14	476	194	0.11	0.41	11.5	8.96	49.8	0.08	0.15	8.88	7.08	0.14	0.05	5.10	3.94
Y	4.86	0.56	0.10	0.01	3.59	0.84	0.01	0.01	0.43	3.52	0.67	0.01	0.01	3.09	0.42	0.01	0.15
Zr	5.06	0.98	1.97	0.45	0.91	0.29	0.11	0.12	0.12	0.31	0.30	0.06	0.06	0.15	0.07	0.03	0.05
Nb	0.02	0.02	0.38	0.21	0.01	0.38	0.27	0.42	0.53	0.01	0.20	0.01	0.01	0.03	0.003	0.01	0.01
Ba	b.d.	b.d.	0.25	0.004	b.d.	0.08	0.03	0.02	93.6	b.d.	0.14	0.01	0.02	0.32	b.d.	0.10	b.d.
La	0.01	0.05	2.21	0.77	b.d.	0.001	0.003	0.002	0.16	b.d.	0.001	0.002	0.001	0.003	b.d.	0.01	0.005
Ce	0.27	0.90	9.62	4.02	0.01	0.01	0.03	0.01	0.26	0.01	0.01	0.02	0.01	0.01	0.004	0.02	0.01
Pr	0.14	0.31	1.47	0.59	0.01	0.01	0.01	0.004	0.05	0.01	0.01	0.01	0.004	0.003	0.003	0.01	0.01
Nd	1.61	2.32	5.60	1.99	0.19	0.18	0.11	0.03	0.60	0.13	0.14	0.08	0.04	0.08	0.09	0.05	0.07
Sm	0.65	0.54	0.40	0.11	0.31	0.16	0.03	0.01	0.37	0.17	0.17	0.02	0.01	0.14	0.08	0.02	0.03
Eu	0.45	0.28	0.14	0.03	0.31	0.15	0.01	0.004	0.30	0.21	0.15	0.01	0.01	0.19	0.08	0.01	0.03
Gd	0.88	0.40	0.15	0.03	0.54	0.22	0.01	0.01	0.40	0.37	0.21	0.01	0.004	0.39	0.13	0.005	0.05
Tb	0.15	0.04	0.01	0.002	0.10	0.04	0.002	0.001	0.04	0.07	0.03	0.001	b.d.	0.07	0.02	0.001	0.01
Dy	1.02	0.19	0.04	0.002	0.71	0.21	0.005	0.004	0.18	0.63	0.17	0.002	b.d.	0.62	0.12	0.005	0.05
Ho	0.19	0.02	0.004	b.d.	0.14	0.04	b.d.	b.d.	0.02	0.14	0.03	b.d.	b.d.	0.12	0.02	0.001	0.01
Er	0.50	0.04	0.01	0.001	0.39	0.08	b.d.	b.d.	0.02	0.44	0.06	0.001	0.001	0.39	0.04	0.002	0.02
Tm	0.06	0.004	0.001	b.d.	0.05	0.01	b.d.	b.d.	b.d.	0.07	0.01	b.d.	b.d.	0.05	0.004	b.d.	0.001
Yb	0.40	0.02	0.003	b.d.	0.31	0.04	b.d.	b.d.	0.01	0.48	0.04	b.d.	b.d.	0.34	0.02	b.d.	0.01
Lu	0.05	0.002	b.d.	b.d.	0.04	0.004	b.d.	b.d.	b.d.	0.07	0.004	b.d.	b.d.	0.05	0.002	b.d.	0.001
Hf	0.13	0.02	0.07	0.03	0.04	0.01	0.02	0.02	b.d.	0.01	0.01	0.01	0.01	0.01	0.004	0.01	0.01
Ta	b.d.	0.001	0.03	0.01	b.d.	b.d.	0.002	0.004	0.002	b.d.	0.004	b.d.	b.d.	0.001	b.d.	b.d.	b.d.
Pb	0.01	0.01	1.39	0.49	0.01	b.d.	0.01	0.04	6.22	0.01	0.01	0.01	0.01	0.06	b.d.	0.08	0.11
Th	0.001	0.01	0.11	0.04	b.d.	b.d.	b.d.	b.d.	0.01	b.d.	0.01	0.003	b.d.	0.001	b.d.	b.d.	b.d.
U	0.01	0.03	0.03	0.01	b.d.	b.d.	b.d.	b.d.	0.005	b.d.	0.002	b.d.	b.d.	0.001	b.d.	b.d.	b.d.
Eu*	1.83	1.87	1.80	1.70	2.31	2.48	2.10	1.41	2.39	2.54	2.32	2.20	2.95	2.51	2.42	2.38	2.15

b.d. bellow detection limit.
p - primary; e- exsolved.

range broadly, decreasing in abundance from large garnets with flat HREE patterns (Sm/Yb_N ~1), to exsolved garnets with more fractionated HREE (Sm/Yb_N >>1). All garnets have positive Eu (Eu* 1.83–2.65) and negative Sr (Sr* 0.02–0.35) anomalies. Zoisite patterns are significantly enriched in LREE compared to exsolved garnet but with similar MREE and slightly lower HREE. It registers similar positive Eu*–2.39 and complementary Sr* – 3.77 anomalies.

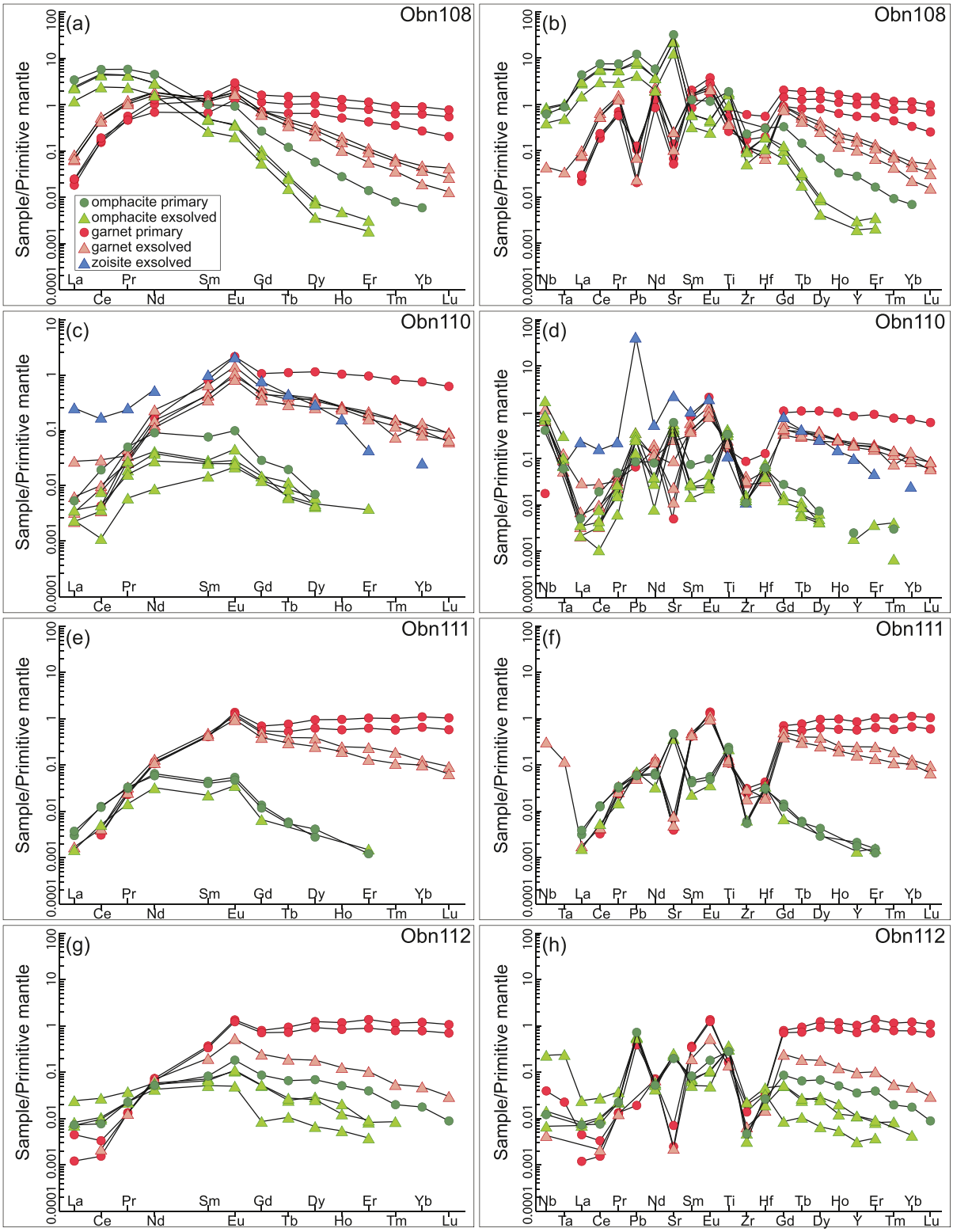

Fig. 6. REE and extended trace element patterns in clinopyroxene, garnet and zoisite, normalized to the primitive mantle values (McDonough and Sun, 1995). There is a wide variability between primary, non-exsolved omphacite and garnet, and the host omphacite after exsolution and the exsolved garnet, respectively. We observe a gradual depletion in HREE proportional to the abundance of exsolutions.

4.4. Water content

4.4.1. Infrared spectroscopy

Both oriented and unoriented omphacite show typical OH vibrational bands at 3620–3613, 3530 and 3440–3430 cm^{-1} (Koch-Müller et al., 2004; Libowitzky and Beran, 2006), with variations in intensity and peak height caused by different grain orientation (Fig. 7 and Supplementary Fig. 4). The OH band at around 3613 cm^{-1} is

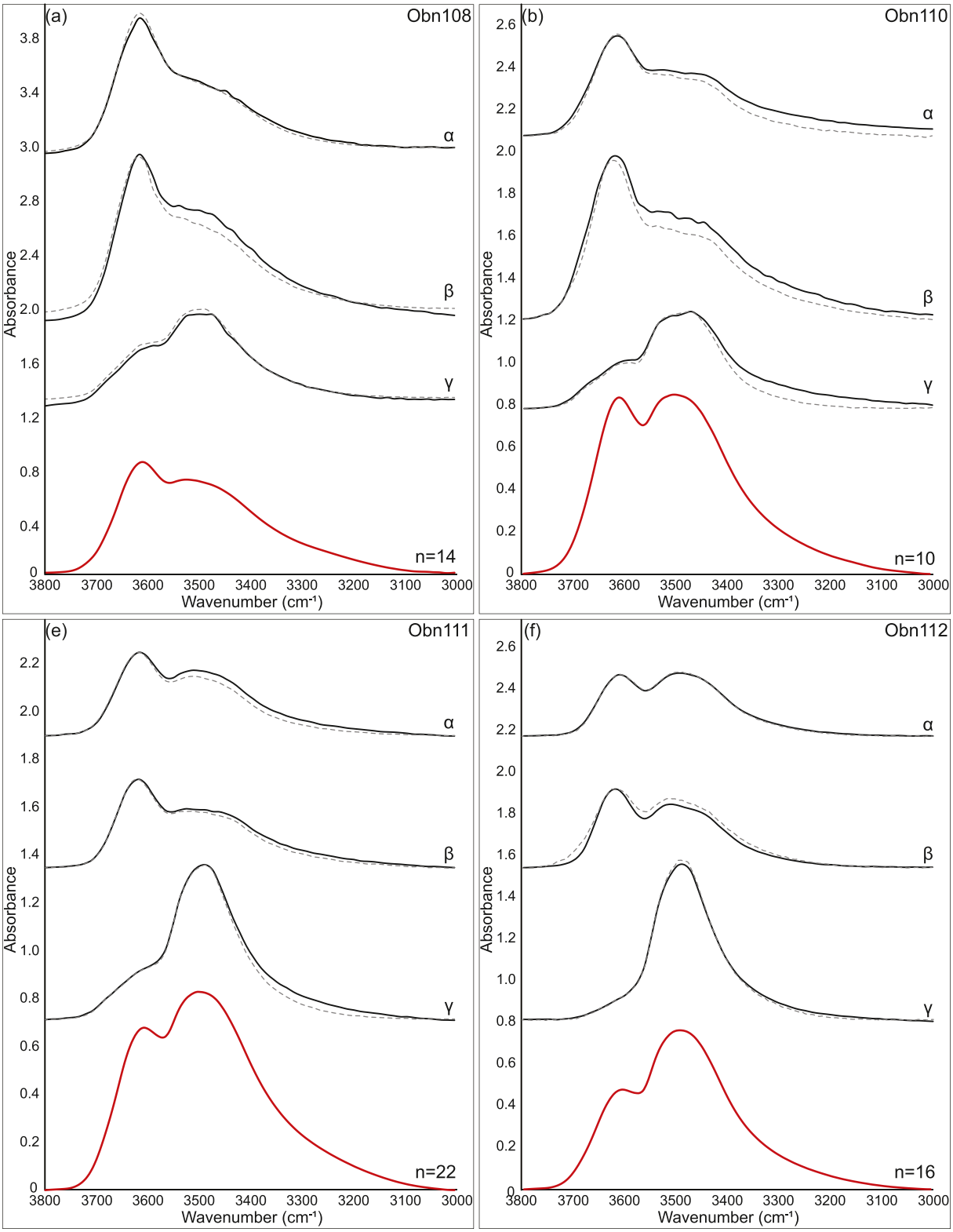

Fig. 7. Infrared spectra of omphacite in the range 3000–3800 cm^{-1}. Spectra are offset for clarity. Samples Obn108, Obn110 and Obn111 show main absorption band at 3620–3613 cm^{-1}, whereas sample Obn112 shows most intense absorption band at 3485 and 3436 cm^{-1}. Solid black line corresponds to initial spectra of oriented crystals, dotted black line corresponds to spectra after samples were heated at 500°C for 12h, and red line corresponds to average spectra of unoriented analyses. (For interpretation of the references to colour in this figure legend, the reader is referred to the web version of this article.)

prominent when the polarization of the electric field vector **E** is parallel to the crystallographic **c** and **a** axes (**E**//**c** (β direction), **E**//**a** (α direction)), while the two bands around 3530 and 3430 cm^{-1} dominate parallel to the crystallographic **b** axis (**E**//**b** (γ direction)). In all four samples, the 3620–3613 and the 3530 cm^{-1} bands appear to be strong, which is uncommon if compared to most previous studies on omphacite (Koch-Müller et al., 2007). This is likely due to omphacite composition, such as particularly high Fe^{3+} content (Bromiley and Keppler, 2004). There are no sharp amphibole bands around 3670–3680 cm^{-1} and there is no marked difference among the absorptions along the three polarizing directions to suggest omphacite contains topotactic sheet silicates overlapping with the peak at 3610 cm^{-1} as it was previously reported for similar samples (Koch-Müller et al. (2004) and references therein). The oriented grains show no significant difference between the initial spectra and the one after the crystals were heated in air, for 12h at 500°C (Fig. 7).

The water content as OH calculated for the omphacite varies with the extinction coefficient used (Table 3). The values calculated with the wavenumber dependent calibration of Libowitzky and Rossman (1997) range from 864 to 1505 ppm, intermediate between those obtained with absorption coefficients of Bell et al. (1995) and of Koch-Müller et al. (2007). The contents calculated based on oriented grains is within error from those based on unoriented grains, attesting to their reliability. These estimates are in general agreement with those of similar samples in the literature 675–1496 ppm (Huang et al., 2014), 43–870 ppm (Peslier, 2010), 31–514 ppm (Koch-Müller et al., 2004). Most large garnet grains do not contain detectable water and only two coarse garnet exsolutions from sample Obn110 were large enough for infrared analysis. These show a distinct, main peak at 3680–3687 cm^{-1} (Fig. 8) overlapping absorption bands previously described for water-rich grossular garnet (Kurka et al., 2005; Phichaikamjornwut et al., 2012; Rossman and Aines, 1991). Nevertheless, the overall shape of the spectra and the notable absence of more dominant grossular peaks is uncommon. The garnet exsolutions yield 600–956 ppm. Whole rock water estimates for the eclogites based on the omphacite content using the Libowitzky and Rossman (1997) calibration yield ~320 ppm for bimineralic eclogite Obn108 and ~1015 ppm, 690 ppm and 505 ppm for the three corundum-bearing eclogites Obn110, Obn111 and Obn112 respectively (Table 3).

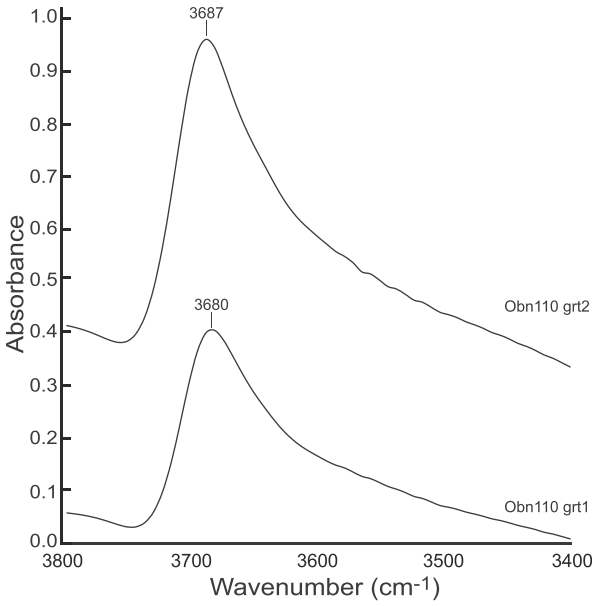

Fig. 8. Representative infrared spectra of exsolved garnet, in the range 3400–3800 cm^{-1}. Spectra are offset for clarity and show main peaks at 3687–3680 cm^{-1}.

4.4.2. *Secondary ion mass spectrometry*

The water content estimated for total hydrogen determined by SIMS is reported by Moine et al. (2020) to be 4850 ± 340 ppm wt. H_2O ($n = 6$) in sample Obn110. This is significantly higher than the FTIR estimates and was previously explained by hydrogen being incorporated under different forms than OH, such as H_2, remaining largely undetected by IR spectroscopy (Moine et al., 2020). Such discrepancies were also previously reported in eclogites and magmatic clinopyroxene by Chen et al. (2011), Kovacs et al. (2016).

The hydrogen profile (Fig. 9) shows a relatively homogeneous H_2O distribution in the host omphacite (1115–1305 ppm wt. H_2O), with a significant, localized increase in concentration at the border with the exsolved lamellae, caused by the inability of the exsolved phases (600–960 ppm wt. H_2O) to accommodate all the hydrogen available.

Table 3
Estimated water content of omp (omphacite), garnet exsolutions and whole rock, calculated based on the estimated mineral modal abundance (for Obn110 1% zoisite and 1% garnet exsolutions are assumed) and ompa. Total hydrogen values are from e - Moine et al. (2020).

		Water Content (ppm weight H_2O)						
Sample	n	omp[a] ± 20%	omp[a] ± 20%*	omp[b] ± 20%	omp[c] ± 20%	calculated whole rock	exsolved garnet[d]	Total hydrogen (SIMS)[e]
Obn108	14	1379 ± 276	–	1584 ± 317	1333 ± 267	317		
Obn108–1	oriented	1494 ± 299	1517 ± 303	1375 ± 275	1158 ± 232	344		
Obn108–2	oriented	1317 ± 263	1113 ± 223	1286 ± 257	1083 ± 217	303	–	–
Obn108–3	oriented	1394 ± 279	1323 ± 265	1448 ± 290	1219 ± 244	321		
Obn110	10	1343 ± 269	–	1309 ± 262	1102 ± 220	973		
Obn110–1	oriented	1320 ± 264	1115 ± 223	1229 ± 246	1034 ± 207	960	600–956	4850 ± 340
Obn110–2	oriented	1505 ± 301	1305 ± 261	1448 ± 290	1219 ± 244	1066		
Obn111	22	1452 ± 290	–	1491 ± 298	1255 ± 251	828		
Obn111–1	oriented	1217 ± 243	1111 ± 222	1209 ± 242	1018 ± 204	694	–	–
Obn111–2	oriented	1194 ± 239	844 ± 169	1136 ± 227	957 ± 191	681		
Obn112	16	1013 ± 203	–	1062 ± 212	894 ± 179	588		
Obn112–1	oriented	880 ± 156	875 ± 176	849 ± 170	715 ± 143	510	–	–
Obn112–2	oriented	864 ± 153	873 ± 175	1165 ± 233	981 ± 196	501		

n - number of grains analysed.
[a] - calibration by Libowitzky and Rossman (1997).
[b] - calibration by Bell et al. (1995).
[c] - calibration by Koch-Müller et al. (2007).
[d] - calibration by Rossman and Aines (1991).
[*] after heating sample at 500 °C, for 12 h.

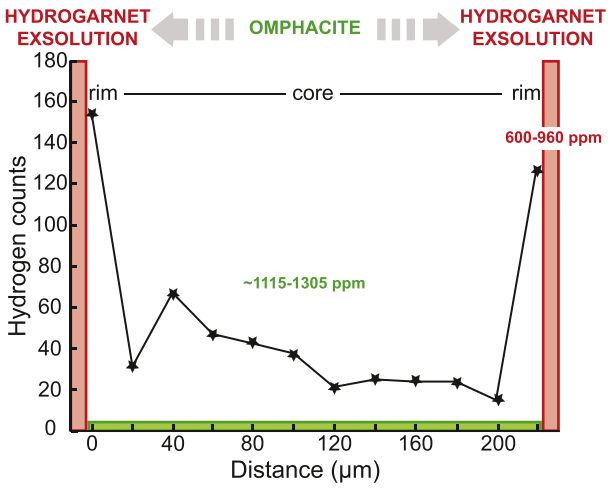

Fig. 9. Hydrogen SIMS profile as proxy for water content in host omphacite marked by green (sample Obn111), in between exsolved hydrogarnet lamellae marked by red. Water content locally increases (3×) towards the exsolved lamellae, as garnet can accommodate less hydrogen in its structure, than omphacite. The horizontal axis corresponds to successive 20 μm steps. The vertical axis represents a raw number of counts and not directly H concentrations. (For interpretation of the references to colour in this figure legend, the reader is referred to the web version of this article.)

5. Discussion

5.1. Exsolution reactions

Garnet exsolution textures in pyroxene, similar to those reported here, have been previously described in eclogites (Dobosi et al., 2007; Harte and Gurney, 1975; Jagoutz, 1988; Jerde et al., 1993; Qi et al., 1997), grosspydites (Sautter and Harte, 1988; Sautter and Harte, 1990; Smyth et al., 1989; Sobolev et al., 1968), websterites (Xu et al., 2004), peridotites (Spengler et al., 2012) and xenocrysts (Aoki et al., 1980) from kimberlites and orogenic massifs all over the world. The typical textural patterns are described as oriented lamellae, lenses, blebs and coronae analogous to the ones identified in this study. The orientation of the lamellae is crystallographically controlled. Through single crystal X-ray diffraction Aoki et al. (1980) determined the topotaxial transition between clinopyroxene and garnet (e.g. [001]Cpx || [111]Grt) subsequently confirmed by Spengler et al. (2012) through Electron backscatter diffraction (EBSD).

At the core of the garnet-clinopyroxene solid solution is the substitution:

$$2Al^{3+} = Si^{4+} + M^{2+} \quad (1)$$

within a precursor superaluminous (Tschermak) pyroxene (Spengler et al., 2012). Thus, the main mineral reactions responsible for garnet exsolution can be formulated as:

$$\underset{\text{diopside}}{CaMgSi_2O_6} + \underset{\text{CaTs}}{CaAl_2SiO_6} = \underset{\text{grossular}-\text{rich garnet}}{Ca_2MgAl_2Si_3O_{12}} \quad (2)$$

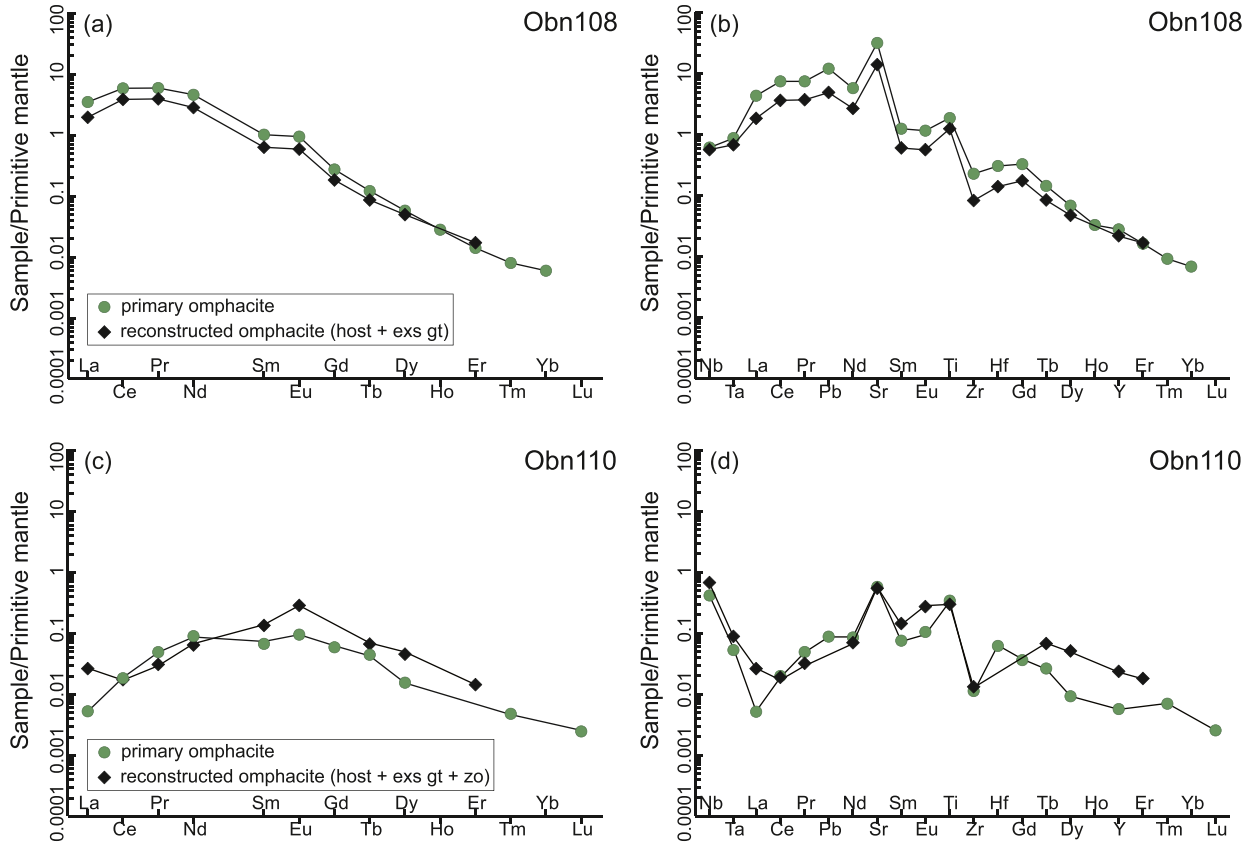

Fig. 10. REE and extended trace elements patterns of large, non-exsolved omphacite (green) and recalculated omphacite (black) from sample Obn108 (a-b) and Obn110 (c-d). The reconstructed composition is based on host omphacite and exsolved garnet for Obn108 and host omphacite, exsolved garnet and zoisite for Obn110. (For interpretation of the references to colour in this figure legend, the reader is referred to the web version of this article.)

$$\underset{\text{diopside}}{2CaMgSi_2O_6} + Al_2Si^{-1}Mg^{-1} = \underset{\text{grossular}-\text{rich garnet}}{Ca_2MgAl_2Si_3O_{12}} \quad (3)$$

Reaction (2) is derived from those suggested by Aoki et al. (1980), Gasparik (1984), Gasparik and Lindsley (1980), and reaction (3) from those suggested by Qi et al. (1997), (Sautter and Harte, 1988), Sautter and Harte (1990). It is inferred that Ca- (grossular-) rich garnet is exsolved at the expense of the Tschermak fraction and Al, with limited consumption of Si and Mg from the host omphacite (Wood and Banno, 1973). This is supported by the decrease in Ca-Tschermak from the non-exsolved to the demixed omphacite grains (by up to 44% in sample Obn110 exhibiting numerous exsolutions, and by 14% in sample Obn112 with fewer exsolutions, see Appendix B).

$$\underset{\text{diopside}}{2CaMgSi_2O_6} + \underset{\text{CaTs}}{2CaAl_2SiO_6} + \underset{\text{structural water}}{Si_2AlMg^{-1} + (OH)} = \underset{\text{garnet}}{Ca_2MgAl_2S_3O_{12}} + \underset{\text{zoisite}}{Ca_2Al_3Si_3O_{12}(OH)} \quad (4)$$

$$\underset{\text{H}-\text{jd (omp)}}{4HAlSi_2O_6} + \underset{\text{Ca}-\text{Ts}}{10CaAl_2SiO_6} + \underset{\text{diopside}}{2CaMgSi_2O_6} + \underset{\text{H}-\text{di (omp)}}{CaH_2Si_2O_6} + Ca_3Mg_{2^-} + 2(OH) = \underset{\text{zoisite}}{8Ca_2Al_3Si_3O_{12}(OH)} \quad (5)$$

The solubility of the Tschermak molecule in clinopyroxenes increases with increasing temperature and/or decreasing pressure (Gasparik, 1984). Due to this compositional dependency, garnet exsolutions may form due to temperature decrease, pressure increase or any combination of the two (Jerde et al., 1993). PT estimates from previous studies, based on local equilibrium of the exsolution lamellae with the reconstructed and the host pyroxene respectively, indicate that the exsolutions formed by slow cooling (from ~1300–1450 °C to ~950–1050 °C) at nearly constant pressure (3.5–4.0 GPa, (Aoki et al., 1980, Dobosi et al., 2007, Harte and Gurney, 1975, Smyth et al., 1989).

5.1.1. Major and trace element distribution

Major element analyses show higher Ca-content in the exsolved garnet compared to the large, matrix garnet (by up to ~9 wt% CaO). As the exsolved garnet grows, it consumes Al and Ca from the host omphacite (see reactions (1) and (2)), causing a local increase in Si and Mg (Fig. 5). The Al content drops significantly adjacent to the garnet lamellae, with a concave-downward chemical gradient towards and in-between the exsolutions. Less marked, Si content slightly increases towards the exsolutions, drawing complementary concave-upward diffusion gradients. Similar trends were previously described by Dobosi et al. (2007), Jerde et al. (1993), Qi et al. (1997), Xu et al. (2004). Al diffusion coefficient in clinopyroxene is lower than for the other cations which explains why Al diffusion profiles are partly preserved, whereas variations of faster-diffusing cations were completely erased by re-equilibration within the host omphacite. This is consistent with the observed preservation of Al compositional gradients, and further implies that the lamellae growth was controlled by the Al diffusion in the pyroxene (Sautter and Harte, 1990). Assuming a measured distance between two exsolved lamellae of 160 μm, clinopyroxene diffusion coefficient of 3.7×10^{-21} m^2/s for Al (Cherniak and Dimanov, 2010) and 10^{-19} m^2/s (Zhang et al., 2009), it would have taken ~683 Ma and 25 Ma respectively, for the compositional profiles to be equilibrated ("erased"). We therefore infer the preservation of these compositional gradients is consistent with eclogites being exhumed by the kimberlite shortly after exsolution.

Contrary to monophasic garnet lamellae, garnet-zoisite exsolutions in Al-rich clinopyroxenes have only been previously mentioned by Xu et al. (2004) in garnet-clinopyroxenite xenoliths in the Xuzhou region, China. Similar to reactions (1) and (3), the exsolution of zoisite can be written very simplified as:

with the simultaneously exsolved garnet acting as the source and sink for Si, Al and Mg respectively. Or as:

case in which preferential endmembers from omphacite are consumed along with different hydrogen speciations. It must be noted these reactions are oversimplified, as the complexity of the system behind the exsolution textures is highly underdetermined.

The major element net transfer between the exsolved garnet ± zoisite assemblage and the host clinopyroxene is recorded in the trace element patterns with complementary fractionation and anomalies of Sr, Ti and Pb (e.g., positive in cpx and negative in grt and zo) (Fig. 6). With increasing exsolution degrees, the host clinopyroxene is depleted in elements compatible in garnet and zoisite (e.g., HREE, Y). Similar fractionation during garnet exsolution from clinopyroxene was previously described in Obnazhennaya eclogites by Dobosi et al. (2007), who argued for a diffusion-controlled nucleation in an isochemical system. The trace element composition of the precursory omphacite was calculated for the bimineralic eclogite Obn108 and corundum-bearing eclogite Obn110 that contains zoisite. The modal abundances assumed for the host and exsolved phases were of omp_{85}–gt_{15} for Obn108 and omp_{85}–gt_5–zo_{10} for Obn110, estimated from Fig. 3. The REE and extended trace elements patterns for the reconstructed compositions and the non-exsolved analysed omphacites are compared in Fig. 10. For both samples the compositions are identical within error, in agreement with both garnet and zoisite having formed in an isochemical system from an initial omphacite, such as it was inferred for similar textures (e.g. Jagoutz (1988), (Sautter and Harte, 1988; Sautter and Harte, 1990)).

5.1.2. Zoisite stability in the upper mantle

Although zoisite is a common primary mineral in low-pressure eclogite facies rocks, associated with Al-rich phases and high water activity (Deer et al., 1986), it was previously reported in mantle xenoliths only as the low pressure alteration product of lawsonite (Sobolev et al., 1968). In natural samples, zoisite exsolutions in clinopyroxene were described in lower crust xenoliths (Xu et al., 2004), stable at lower PT conditions (620°–780 °C, 1.5–2GPa) compared to those recorded by the Obnazhennaya eclogites (850–1140 °C, 3–4 GPa).

Multi-anvil experiments coupled with thermodynamic modelling by Poli (2016) nevertheless place the zoisite-to-lawsonite transition at ~6.8 GPa and ~ 950 °C, well above, and thus including the calculated temperature range for the Obnazhennaya samples. This is further supported by experimental work of Poli and Schmidt (1998) who showed

that zoisite is stable up to 7GPa at ~1050 °C under Al_2O_3 + H_2O-saturated experimental conditions. These theoretical and experimental observations support zoisite stability in the upper mantle, for a specific compositional range. The major element composition of the precursory omphacite in the corundum and zoisite-bearing sample Obn110 was recalculated assuming the average composition of the host omphacite, exsolved garnet and zoisite and the same modal abundances as for the trace elements. The composition obtained is within 0.1–1.4 wt% in agreement with the average composition of the non-exsolved omphacite. The Al_2O_3 + H_2O-saturated prerequisite for zoisite stability at the PT conditions where the eclogites are equilibrated in the upper mantle are satisfied within the closed omphacite system (18.50–17.10 wt% Al_2O_3, 4850 ± 340 ppm wt. H_2O (Moine et al., 2020)).

5.1.3. Zoisite as product of fluid overprint

An alternative explanation for the presence of zoisite is that it formed at the expense of the exsolved garnet, through fluid overprint. Assuming an external hydrous component infiltrated prior to (or during) the kimberlite eruption, but postdating garnet exsolution however, raises significant issues. The preservation of the major element diffusion gradients at mantle conditions would be highly improbable given the accelerated Si—Al diffusion in the presence of OH (Goldsmith, 1986). It is equally difficult from a kinetic point of view to explain how this fluid was channelled solely along, and overprinted the micrometre-sized garnet lamellae, forming an imbricated garnet-zoisite microtexture (Fig. 3), without destabilizing the host omphacite and the sample throughout. From a mass-balance point of view, any external fluid would likely carry other elements in addition to hydrogen, which would be observed in trace element composition of the exsolved phases, relative to the non-exsolved. However, both the major and trace element recalculated composition of the precursory omphacite is identical within error to that of the non-exsolved omphacite (Fig. 10). This raises a question of what would be the nature and source of such a fluid. Kimberlite-derived metasomatism, has distinct features, such as interstitial amphiboles, kelyphitic destabilization of the omphacite, interstitial rutile, melt inclusions, K_2O > 0.9 wt% in omphacite and enriched REE composition (Gréau et al., 2011). None of these features are observed in the studied samples.

Alternatively, hydrogen may have diffused from the host omphacite postdating garnet exsolution, and led to zoisite formation. Hydrogen solubility in omphacite decreases during decompression (Skogby et al., 2016), whereas garnet exsolution is favoured by increasing pressure or decreasing temperature (Gasparik, 1984). In this model, the major element diffusion profiles (Fig. 5) are 'frozen in' during garnet growth shortly (less than 25 Ma) before the fast exhumation of the eclogites (18–92 m/s, Peslier et al. (2008)). Although this model cannot be fully ruled out, assuming zoisite growth postdates garnet formation fails to account for the euhedral zoisite crystals within the lamellae (Fig. 3e). In terms of trace elements balance, assuming garnet was first exsolved from an initial omphacite and subsequently transformed into zoisite, the trace elements would have been partitioned between two phases, and not all the three as it is observed (Fig. 6c–d).

We posit that unlike in assemblages from crustal settings, the most likely explanation for zoisite described in this study is its exsolution directly from omphacite in a closed system, with no fluid infiltration based on (i) Al, Si and Mg diffusion profiles in-between the exsolved garnet+zoisite lamellae showing depletion of Al—Si and enrichment in Mg in the adjacent host omphacite, caused by their respective incorporation and expulsion from the zoisite structure (Fig. 5); (ii) partitioning of trace elements between host omphacite, exsolved garnet and exsolved zoisite indicating that garnet and zoisite exsolutions formed concomitantly (Fig. 6 c–d); and (iii) the recalculated precursory omphacite matching the non-exsolved omphacite (Fig. 10 c–d).

5.2. Water in omphacite

The average water content determined as OH for the oriented grains (872–1413 ppm) is within 20% error in agreement with the content determined for the unoriented grains (1013–1452 ppm). To verify whether there is a contribution to the spectra from minor fluid inclusions, the oriented crystals were analysed in the near-Infrared range and no molecular water peaks were detected. Additionally they were re-analysed after being heated at 500 °C in air for 12 h, and the new spectra were compared to the initial results (Fig. 7). The estimated water content after heating (874–1318 ppm) is within the same range as the initial estimates. Although it would be possible for some well isolated fluid inclusions to be able to survive this experiment, most nanometre-sized fluid inclusions wouldn't have survived and a significant decrease in the water content was to be expected.

Different OH defects may coexist within the structure of NAMs (e.g., atomic substitutions, vacancies, dislocations in distorted lattices Demouchy and Bolfan-Casanova (2016)), controlled by both internal, i.e. chemical, and external factors, such as pressure, temperature, iron content, oxygen and water fugacity (Peslier et al., 2002; Skogby et al., 2016). In the pyroxene structure, the O2 oxygen is the most favourable site to incorporate OH, as it is highly under-bonded according to its Pauling bond strength (Skogby et al., 2016). The excess charge may be compensated by either M2 cation vacancies or charge-deficient substitutions in the tetrahedral site (Ingrin and Skogby, 2000).

The presence of two differently pleochroic groups of absorption bands indicates that at least two types of hydrogen locations may coexist (Ingrin and Skogby, 2000). When the OH dipole is oriented parallel to O2···M2 the lower wavenumber bands are strong (e.g. 3460 cm^{-1}, Ingrin and Skogby (2000)); when it is oriented parallel to O2···O3 the dominating band shifts to higher wavenumbers (e.g. 3620 cm^{-1} (Skogby, 2006)). Accordingly, it might be that samples Obn108, Obn110 and Obn111 that have an intense peak for the 3620–3613 cm^{-1} band, taking into account grain orientation (Fig. 7, Supplementary Fig. 4) likely accommodate OH by substituting Si^{4+} with trivalent cations (e.g. Al^{3+}), whereas sample Obn112 that has an intense peak in the 3436 and 3485 cm^{-1} range likely accommodates OH by M2 cation vacancies and (e.g. Na^{+}–Ca^{2+}) charge deficient substitutions (Bromiley and Keppler, 2004; Koch-Müller et al., 2004; Libowitzky and Beran, 2006). Although previous studies relate the position and intensity of characteristic peaks to vacancies and abundances of certain elements (Al, Fe^{3+}, Ti, Na; (Peslier et al., 2002) and references therein), we do not observe direct correlations of dominant absorption bands and specific compositions (Appendix F). This could be due to significant differences in the PT equilibrium conditions and overall composition between our samples and omphacites from previous studies. Alternatively, the limited number of samples might obscure possible correlations.

The hydrogen distribution profile (Fig. 9) determined by SIMS, was taken in the host omphacite in-between two exsolved lamellae. The steep increase in hydrogen counts restricted to the vicinity of the exsolution is likely caused by the low hydrogen solubility in garnet compared to omphacite (Demouchy and Bolfan-Casanova, 2016). This is also seen for Si and Mg (Fig. 5). Assuming the same modal abundance used above for major and trace elements reconstruction, a minimum of 2035 ppm of water (independent of hydrogen configuration) is required to form the exsolved garnet and zoisite. The bulk water content for omphacite in corundum and zoisite-bearing sample Obn110 was reported by Moine et al. (2020) to be 4850 ± 340 ppm determined by SIMS or 4850 ± 260 ppm by TC/EA-IRMS. Both independent types of analyses detect all hydrogen configurations. They argue the difference between the bulk water content and that determined as OH is largely accounted for by water as H_2, detected albeit weakly at 4100 cm^{-1}. This is supported by consistent results in a suit of 8 additional mantle omphacites from the Roberts Victor kimberlite (Moine et al., 2020), as well as by similar previous studies (Chen et al., 2011; Kovacs et al., 2016). Alternatively, the discrepancies between the two analytical techniques could in part be

explained by an imprecise calibration of the FTIR spectra. Such high water contents could easily account for the hydrogen consumed by the garnet and zoisite exsolutions.

5.3. Water in garnet

Studies on both synthetic and natural garnet report the presence of various OH^- absorption bands in the IR spectra, controlled largely by the garnet composition (Aines and Rossman, 1984; Bell et al., 1995; Bell and Rossman, 1992; Phichaikamjornwut et al., 2012; Rossman and Aines, 1991). Such that IR spectra of Mn^{2+}-rich garnets have strong absorption bands centred near 3640 and 3600 cm^{-1}, Fe^{2+}-rich garnets near 3540 and 3470 cm^{-1}, Mg^{2+}-rich garnets near ~3670 cm^{-1} (Aines and Rossman, 1984) and Ca-rich garnets near ~3660 and 3600 cm^{-1} (Rossman and Aines, 1991). The most common type of OH incorporation is the hydrogarnet substitution $(H_4O_4)^{4-} = (SiO_4)^{4-}$ (Aines and Rossman, 1984). However, the wide range in specific absorption bands of different garnet varieties (Rossman and Aines, 1991) indicates that additional replacement modes could also account for OH^-, such as cation vacancies compensated by $[SiO_3(OH)]$, $(Al^{3+}–H^+) = Si^{4+}$, $\{H^+–H^+, Li^+–H^+\} = \{Ca^{2+}, Mg^{2+}, Fe^{2+}, Mn^{2+}\}$ (Geiger and Rossman (2020) and references therein). The strong, sharp absorption band near 3680–3687 cm^{-1} seen in the exsolved garnet lamellae (Fig. 8) could be thus explained by the hydrogarnet substitution (Kurka et al., 2005) and $\{H^+–H^+\}$ replacing $\{Ca^{2+}\}$, but other forms of structural defects and combinations cannot be ruled out. Alternatively, peaks at 3687–3688 cm^{-1} in grossular were attributed to defects associate to the substitution of Si^{4+} by $(OH^+ + 3F^+)$ (Mosenfelder et al., 2022). Although we do not have any reason to expect high F concentrations in the analysed garnets, this possibility cannot be ruled out.

Whereas OH-peaks at 3680–3687 cm^{-1} were previously reported in other grossular-rich garnets (Kurka et al., 2005), the shape of the spectra and the absence of other specific peaks are uncharacteristic (Fig. 8). It was suggested similar peaks could be due to nanometre-sized inclusions of an unknown OH-rich mineral (Geiger and Rossman, 2020). Assuming such a hydrous mineral could be found in the garnet lamellae, and remain optically undetected, the FTIR spectra would show an overlap between the characteristic OH peaks of garnet and those of the unknown mineral, which is not the case. Moreover, for a thickness of 500 μm as that of the garnets showing the 3680–3687 cm^{-1} peak (Fig. 8), a hydrous mineral would yield an absorbance significantly higher than 0.4–0.6% (likely >2%). Based on these reasons and the intragrain chemical homogeneity of the exsolved garnet (Table 1, Appendix B), this explanation seems unlikely.

There is a strong discrepancy between the large anhydrous garnet, and garnet exsolved by omphacite, the latter exhibiting high amount of water. The large garnet is pyrope-rich ($Py_{56}Alm_{17}Grs_{27}$ average composition), whereas garnet exsolutions are grossular-rich ($Py_{36}Alm_{13}Grs_{51}$ avg. comp). Due to the different occupancy and size of the dodecahedron structural site, it has been noted that the hydrogarnet substitution is less stable in pyrope garnets than in grossular, such that pyrope-rich garnets are capable of storing only small amounts of water in the upper mantle (Bell and Rossman, 1992; Demouchy and Bolfan-Casanova, 2016). Other possible factors that may cause this variation are water fugacity, pressure and availability of structural defects. The differences in water content between coexisting garnet and omphacite are likely due to different solubility and diffusion coefficients of hydrogen in the two minerals.

5.4. Water in mantle eclogites: Origin and preservation

Hydrogen concentration in mantle NAMs has been extensively studied, mostly in peridotite xenoliths due to their predominance. Mantle metasomatism prior to the kimberlite eruption seemed the most probable source for water (Doucet et al., 2014), as no correlation was found with subduction-zone proximity (Peslier et al., 2002). Mantle eclogites are derived from recycled oceanic crust (Radu et al., 2019) and can store significantly higher water contents (bulk estimates of ~320–970 ppm, Table 3), than the surrounding mantle (90–290 ppm for Udachnaya peridotites (Doucet et al., 2014)). Trace amounts of water can be trapped in NAMs and preserved even at eclogite facies conditions (Katayama et al., 2006), or high-pressure hydrous minerals (lawsonite, phengite and zoisite-clinozoisite) can be the water source during eclogitisation in the upper mantle (Maruyama and Okamoto, 2007; Poli and Schmidt, 1998; Vitale-Brovarone et al., 2014). Additionally, faults and fractures of the oceanic slab preceding subduction may serve as conduits for hydrothermal fluids, that can introduce significant amounts of water into the upper mantle via alteration biproducts (Li et al., 2008). The incorporation and preservation of water in omphacite is facilitated by increased hydrogen solubility with increasing pressure (Keppler and Bolfan-Casanova, 2006) up to ~3.5–4 GPa, overlapping with the PT estimates for the Obnazhennaya eclogites.

Hydrogen rapidly diffuses through NAMs at high temperatures (> 800 °C) and water gain from the H_2O-rich kimberlite magma, or water loss due to decompression can be expected (Demouchy et al., 2006). If water was added to the xenoliths from the entrapping magma, higher hydrogen contents would be expected for the rims, than in the core of the samples. Previous studies of peridotite xenoliths have noticed the opposite for olivine crystals, indicating water loss and not water gain, while the associated garnets and pyroxene were completely unaffected (Demouchy et al., 2006; Doucet et al., 2014; Peslier and Luhr, 2006). The fast ascent rate of kimberlite (a few hours (Peslier et al., 2008)) combined with the slow hydrogen diffusion rate in pyroxene (Demouchy et al., 2011; Ingrin and Skogby, 2000) prevents both water addition from the kimberlite and water loss due to decompression. As such, mantle omphacites are believed to preserve their initial water content (Kovacs et al., 2016; Moine et al., 2020; Sundvall and Stalder, 2011).

6. Conclusions

This study describes four non-metasomatized eclogite xenoliths from the Siberian craton that contain garnet and garnet-zoisite in exsolution textures hosted by omphacite. Water content of non-exsolved omphacites is estimated to be ~870–1415 ppm as OH and 4850 ppm as total hydrogen. Specific major and trace elements, together with hydrogen, seem to be preferentially consumed by the exsolutions, compensated by their depletion in the host omphacite. Related diffusion profiles were 'frozen in' indicating that the exsolution took place shortly (<25 Ma) before the kimberlite eruption. Based on the present findings, the zoisite formation most likely accompanied garnet exsolution from an Al, water-rich omphacite, within the upper mantle.

Assuming this model, zoisite stability at mantle conditions is demonstrated for the first time in natural samples. This opens an avenue for more detailed research into modelling the formation of such exsolution textures and the importance of hydrogen in NAMs for phase transition.

Supplementary data to this article can be found online at https://doi.org/10.1016/j.lithos.2022.106681.

Declaration of Competing Interest

The authors declare that they have no known competing financial interests or personal relationships that could have appeared to influence the work reported in this paper.

Acknowledgements

The authors are grateful to Prof Henrik Skogby and Dr. Simon Schorn for their helpful informal reviews; to Dr. Dirk Spengler, Prof Jörg Hermann and three anonymous reviewers for their comments and ideas; to Prof Emer Herb Helmstaedt and Prof Nadia Malaspina for their editorial handling; and to Colette Guilbaud for the careful and precise

preparation of the thin sections and double polished grains. This research was supported by the Laboratory of Excellence ClerVolc (BM, NB), Jean Monnet University-Saint-Etienne (BM, JYC, IBR) and CNRS-PICS grant (DI). AVG was supported by the Russian Foundation for Basic Research (grantNo 18-05-70064) and AVK and OBO were supported by Russian Federation state assignment projects of IGM SB RAS and of DPMGI SB RAS. This is Laboratory of Excellence ClerVolc contribution n° 528.

References

Agashev, A.M., Pokhilenko, N.P., Tolstov, A., Polyanichko, V.V., Mal'kovets, V.G., Sobolev, N.V., 2004. New age data on kimberlites from the Yakutian Diamandiferous Province. Dokl. Earth Sci. 399, 1142–1145.

Aines, D.R., Rossman, G.R., 1984. Water content of mantle garnets. Geology 12, 720–723.

Alifirova, T.A., Pokhilenko, L., Ovchinnikov, Y.I., Donnelly, C.L., Riches, A.J.V., Taylor, L.A., 2012. Petrologic origin of exsolution textures in mantle minerals: evidence in pyroxenitic xenoliths from Yakutia kimberlites. Int. Geol. Rev. 54, 1071–1092.

Aoki, K.-I., Fujimaki, H., Kitamura, M., 1980. Exsolved garnet-bearing pyroxene megacrysts from some South African kimberlites. Lithos 13, 269–279.

Bell, D.R., Rossman, G.R., 1992. Water in Earth's mantle: the Role of nominally anhydrous minerals. Science 255, 1391–1397.

Bell, D.R., Ihinger, P.D., Rossman, G.R., 1995. Quantitative analysis of trace OH in garnet and pyroxenes. Am. Mineral. 80, 465–474.

Beyer, C., Frost, D.J., Miyajima, N., 2015. Experimental calibration of a garnet–clinopyroxene geobarometer for mantle eclogites. Contrib. Mineral. Petrol. 169.

Blanco, D., Kravchinsky, V.A., Konstantinov, K.M., Kabin, K., 2013. Paleomagnetic dating of Phanerozoic kimberlites in Siberia. J. Appl. Geophys. 88, 139–153.

Bromiley, G.D., Keppler, H., 2004. An experimental investigation of hydroxyl solubility in jadeite and Na-rich clinopyroxenes. Contrib. Mineral. Petrol. 147, 189–200.

Chen, R.-X., Zheng, Y.-F., Gong, B., 2011. Mineral hydrogen isotopes and water contents in ultrahigh-pressure metabasite and metagranite: constraints on fluid flow during continental subduction-zone metamorphism. Chem. Geol. 281, 103–124.

Cherniak, D.J., Dimanov, A., 2010. Diffusion in pyroxene, mica and amphibole. Rev. Mineral. Geochem. 72, 641–690.

Deer, W.A., Howie, R.A., Zussman, J., 1986. Epidote group. In: Rock-Forming Minerals. Longman Group, UK, pp. 4–43.

Deloule, E., Paillat, O., Pichavant, M., Scaillet, B., 1995. Ion microprobe determination of water in silicate glasses: methods and applications. Chem. Geol. 125, 19–28.

Demouchy, S., Bolfan-Casanova, N., 2016. Distribution and transport of hydrogen in the lithospheric mantle: a review. Lithos 402–425.

Demouchy, S., Jacobsen, S.D., Gaillard, F., Stern, C.R., 2006. Rapid magma ascent recorded by water diffusion profiles in mantle olivine. Geology 34, 429–432.

Demouchy, S., Jacobsen, S.E., Gaillard, F., Stern, C.R., 2011. Rapid magma ascent recorded by water diffusion profiles in mantle olivine. Geology 34, 429–432.

Dobosi, G., Kurat, G., Wall, F., Jeffries, T., 2007. Trace element fractionation during exsolution of garnet from clinopyroxene in an eclogite xenolith from Obnazhennaya (Siberia). In: Goldschmidt. Cambridge Publications, Cologne, Germany.

Doucet, L.S., Peslier, A.H., Ionov, D.A., Brandon, A.D., Golovin, A.V., Goncharov, A.G., Ashchepkov, I.V., 2014. High water contents in the Siberian cratonic mantle linked to metasomatism: an FTIR study of Udachnaya peridotite xenoliths. Geochim. Cosmochim. Acta 137, 159–187.

Ellis, D.J., Green, D.H., 1979. An experimental study of the effect of Ca upon garnet-clinopyroxene Fe-Mg exchange equilibria. Contrib. Mineral. Petrol. 71, 13–22.

Feineman, M.D., Ryerson, F.J., DePaolo, D.J., Plank, T., 2007. Zoisite-aqueous fluid trace element partitioning with implications for subduction zone fluid composition. Chem. Geol. 239, 250–265.

Gasparik, T., 1984. Experimentally determined stability of clinopyroxene + garnet + corundum in the system CaO-MgO-Al2O3-SiO2. Am. Mineral. 69, 1025–1035.

Gasparik, T., Lindsley, D.H., 1980. Phase equilibria at high pressure of pyroxenes containing monovalent and trivalent ions. In: Prewitt, C.H. (Ed.), Pyroxenes. Mineralogical Society of America, Washington D.C.

Geiger, C.A., Rossman, G.R., 2020. Micro- and nano-size hydrogarnet clusters and proton ordering in calcium silicate garnet: part I. the quest to understand the nature of "water" in garnet continues. Am. Mineral. 105, 455–467.

Goldsmith, J.R., 1986. The role of hydrogen in promoting Al-Si interdiffusion in albite (NaAlSi3O8) at high pressure. Earth Planet. Sci. Lett. 80, 135–138.

Gréau, Y., Huang, J.-X., Griffin, W.L., Renac, C., Alard, O., O'Reilly, S.Y., 2011. Type I eclogites from Roberts Victor kimberlites: Products of extensive mantle metasomatism. Geochim. Cosmochim. Acta 75, 6927–6954.

Green, D.H., Hibberson, W.O., Kovacs, I., Rosenthal, A., 2010. Water and its influence on the lithosphere–asthenosphere boundary. Nature 467, 448–451.

Griffin, W., Ryan, C.G., Kaminsky, F.V., O'Reilly, S.Y., Natapov, L.M., Win, T.T., Kinny, P. D., Ilupin, L.M., 1999. The Siberian lithosphere traverse: mantle terranes and the assembly of the Siberian Craton. Tectonophysics 310, 1–35.

Harte, B., Gurney, J.J., 1975. Evolution of clinopyroxene and garnet in an eclogite nodule from the Roberts Victor kimberlite pipe, South Africa. Phys. Chem. Earth 9, 367–387.

Huang, J.-X., Gréau, Y., Griffin, W.L., O'Reilly, S.Y., Pearson, N.J., 2012. Multi-stage origin of Roberts Victor eclogites: progressive metasomatism and its isotopic effects. Lithos 161–181.

Huang, J.-X., Li, P., Griffin, W.L., Xia, Q.-K., Gréau, Y., Pearson, N.J., O'Reilly, S.Y., 2014. Water contents of Roberts Victor xenolithic eclogites: Primary and metasomatic controls. Contrib. Mineral. Petrol. 168.

Ingrin, J., Skogby, H., 2000. Hydrogen in nominally anhydrous upper-mantle minerals: concentration levels and implications. Eur. J. Mineral. 12, 543–570.

Ionov, D.A., Doucet, L.S., Xu, Y., Golovin, A.V., Oleinikov, O.B., 2018. Reworking of Archean mantle in the NE Siberian craton by carbonatite and silicate melt metasomatism: evidence from a carbonate-bearing, dunite-to-websterite xenolith suite from the Obnazhennaya kimberlite. Geochim. Cosmochim. Acta 224, 132–153.

Ionov, D.A., Qi, Y.-H., Kang, J.-T., Golovin, A.V., Oleinikov, O.B., Zheng, W., Anbar, A.D., Zhang, Z.-F., Huang, F., 2019. Calcium isotopic signatures of carbonatite and silicate metasomatism, melt percolation and crustal recycling in the lithospheric mantle. Geochim. Cosmochim. Acta 248, 1–13.

Jaffres, B.D.J., Shields, G.A., Wallmann, K., 2007. The oxygen isotope evolution of seawater: a critical review of a long-standing controversy and an improved geological water cycle mode for the past 3.4 billion years. Earth Sci. Rev. 83, 83–122.

Jagoutz, E., 1988. Nd and Sr systematics in an eclogite xenolith from Tanzania: evidence for frozen mineral equilibria in the continental lithosphere. Geochim. Cosmochim. Acta 52, 1285–1293.

Jerde, E.A., Taylor, L.A., Crozaz, G., Sobolev, N.V., 1993. Exsolution of garnet within clinopyroxene of mantle eclogites: major- and trace-element chemistry. Contrib. Mineral. Petrol. 114, 148–159.

Katayama, I., Nakashima, S., Yurimoto, H., 2006. Water content in natural eclogite and implication for water transport into the deep upper mantle. Lithos 245–259.

Keppler, H., Bolfan-Casanova, N., 2006. Thermodynamics of water solubility and partitioning. Rev. Mineral. Geochem. 62, 193–230.

Koch-Müller, M., Matsyuk, S.S., Wirth, R., 2004. Hydroxyl in omphacites and omphacitic clinopyroxenes of upper mantle to lower crustal origin beneath the Siberian platform. Am. Mineral. 89, 921–931.

Koch-Müller, M., Abs-Wurmbach, I., Rhede, D., Kahlenberg, V., Matsyuk, S.S., 2007. Dehydration experiments on natural omphacites: qualitative and quantitative characterization by various spectroscopic methods. Phys. Chem. Miner. 34, 663–678.

Kolesnichenko, M.V., Zedgenizov, D.A., Ragozin, A.L., Litasov, K.D., Shatsky, V.S., 2018. The role of eclogites in the redistribution of water in the subcontinental mantle of the Siberian craton: results of determination of the water content in minerals from the Udachnaya pipe eclogites. Russ. Geol. Geophys. 59, 763–779.

Kovacs, I., Hermann, J., O'Neill, H.S.C., Gerald, J.F., Sambridge, M., Horvath, G., 2008. Quantitative absorbance spectroscopy with unpolarized light: Part II. Experimental evaluation and development of a protocol for quantitative analysis of mineral IR spectra. Am. Mineral. 93, 765–778.

Kovacs, I., Demény, A., Czuppon, G., Lécuyer, C., Fourel, F., Xia, Q.-K., Liu, J., Pintér, Z., Kiraly, E., Török, K., Szabo, A., Deloule, E., Falus, G., Fancsik, T., Zajacz, Z., Sandorné Kovacs, J., Udvardi, B., 2016. Water concentrations and hydrogen isotope compositions of alkaline basalt hosted clinopyroxene megacrysts and amphibole clinopyroxenites: The role of structural hydroxyl groups and molecular water. Contribut. Mineral. Petrol. 171.

Krogh, E., 1988. The garnet-clinopyroxene Fe–Mg geothermometer– a reinterpretation of existing experimental data. Contrib. Mineral. Petrol. 99, 44–48.

Krogh-Ravna, E., 2000. Distribution of Fe2+ and Mg between coexisting garnet and hornblende in synthetic and natural systems: an empirical calibration of the garnet-hornblende Fe-Mg geothermometer. Lithos 265–277.

Kurka, A., Blanchard, M., Ingrin, J., 2005. Kinetics of hydrogen extraction and deuteration in grossular. Mineral. Mag. 69, 359–371.

Li, Z.-X.A., Lee, C.-T.A., Peslier, A.H., Lenardic, A., Mackwell, S.J., 2008. Water contents in mantle xenoliths from the Colorado Plateau and vicinity: Implications for the mantle rheology and hydration-induced thinning of continental lithosphere. J. Geophys. Res. 113.

Libowitzky, E., Beran, A., 2006. The structure of hydrous species in Nominally Anhydrous Minerals: information from polarized IR spectroscopy. Rev. Mineral. Geochem. 62, 29–52.

Libowitzky, E., Rossman, G.R., 1997. An IR absorption calibration for water in minerals. Am. Mineral. 82, 111–1115.

MacGregor, I.D., Carter, J.L., 1970. The chemistry of clinopyroxenes and garnets of eclogite and peridotite xenoliths from the Roberts Victor mine, South Africa. Phys. Earth Planet. Inter. 3, 391–397.

Maruyama, S., Okamoto, K., 2007. Water transportation from the subducting slab into the mantle transition zone. Gondwana Res. 11, 148–165.

Massonne, H.-J., 2012. Formation of amphibole and clinozoisite-epidote in eclogite owing to fluid infiltration during exhumation in a subduction channel. J. Petrol. 53, 1969–1998.

McDonough, W.F., Sun, S.-S., 1995. The composition of the Earth. Chem. Geol. 120, 223–253.

Mei, S., Kohlstedt, D.L., 2000. Influence of water on plastic deformation of olivine aggregates 1. Diffusion creep regime. J. Geophys. Res. 105, 21,457-421,469.

Moine, B.N., Bolfan-Casanova, N., Radu, I.B., Ionov, D.A., Costin, G., Korsakov, A.V., Golovin, A.V., Oleinikov, O.B., Deloule, E., Cottin, J.Y., 2020. Molecular hydrogen in minerals as a clue to intrepret ∂D variations in the mantle. Nat. Commun. 11.

Morimoto, N., 1988. Nomenclature of Pyroxenes. Mineral. Petrol. 39, 55–76.

Mosenfelder, J.L., Von der Handt, A., Withers, A.C., Bureau, H., Raepsaet, C., Rossman, G.R., 2022. Coupled hydrogen and fluorine incorporation in garnet: new constraints from FTIR, ERDA, SIMS and EPMA. Am. Mineral. in press.

Müller, W., Shelley, M., Miller, P., Broude, S., 2009. Initial performance metrics of a new custom-designed ArF excimer LA-ICPMS system coupled to a two-volume laser-ablation cell. J. Anal. At. Spectrom. 24, 209–214.
Nakamura, D., 2009. A new formulation of garnet–clinopyroxene geothermometer based on accumulation and statistical analysis of a large experimental data set. J. Metamorph. Geol. 27, 495–508.
Ohtani, E., Yuan, L., Ohira, I., Shatskiy, A., Litasov, K.D., 2018. Fate of water transported into the deep mantle by slab subduction. J. Asian Earth Sci. 167, 2–10.
Peslier, A.H., 2010. A review of water contents of nominally anhydrous natural minerals in the mantles of Earth, Mars and the Moon. J. Volcanol. Geotherm. Res. 239–258.
Peslier, A.H., Luhr, J.F., 2006. Hydrogen loss from olivines in mantle xenoliths from Simcoe (USA) and Mexico: Mafic alkalic magma ascent rates and water budget of the sub-continental lithosphere. Earth Planet. Sci. Lett. 242, 302–319.
Peslier, A.H., Luhr, J.F., Post, J., 2002. Low water contents in pyroxenes from spinel-peridotites of the oxidized, sub-arc mantle wedge. Earth Planet. Sci. Lett. 201, 69–86.
Peslier, A.H., Woodland, A.B., Wolff, J.A., 2008. Fast kimberlite ascent rates estimated from hydrogen diffusion profiles in xenolithic mantle olivines from southern Africa. Geochim. Cosmochim. Acta 72, 2711–2722.
Phichaikamjornwut, B., Skogby, H., Ounchanum, P., Limtrakun, P., Boonsoong, A., 2012. Hydrous components of grossular-andradite garnets from Thailand: thermal stability and exchange kinetics. Eur. J. Mineral. 24, 107–121.
Pisarevsky, S.A., Natapov, L.M., Donskaya, T.V., Gladkochub, D.P., Vernikovsky, V.A., 2008. Proterozoic Siberia: a promontory of Rodinia. Precambrian Res. 160, 66–76.
Poli, S., 2016. Melting carbonated epidote eclogites: Carbonatites from subducting slabs. Prog. Earth Planet. Sci. 3.
Poli, S., Schmidt, M.W., 1995. H2O transport and release in subduction zones: Experimental constraints on basaltic and andesitic systems. J. Geophys. Res. 100, 22,299-222,314.
Poli, S., Schmidt, M.W., 1998. The high-pressure stability of zoisite and phase relationships of zoisite-bearing assemblages. Contrib. Mineral. Petrol. 130, 162–175.
Pollack, H.N., Chapman, D.S., 1977. On the regional variations of the heat flow, geotherms, and lithospheric thickness. Tectonophysics 38, 279–296.
Qi, Q., Taylor, L.A., Snyder, G.A., Clayton, R.N., Mayeda, T.K., Sobolev, N.V., 1997. Detailed petrology and geochemistry of a rare corundum eclogite xenolith from Obnazhennaya, Yakutia. Russ. Geol. Geophys. 38, 247–260.
Radu, I.B., Moine, B.N., Ionov, D.A., Korsakov, A., Golovin, A.V., Mikhailenko, D., Cottin, J.-Y., 2017. Kyanite-bearing eclogite xenoliths from Udachnaya kimberlite, Siberian craton, Russia. Bull. Soc. Géol. France 188, 75–84.
Radu, I.B., Harris, C., Moine, B.N., Costin, G., Cottin, J.-Y., 2019. Subduction relics in the subcontinental lithospheric mantle, evidence from δ18O variations in eclogite xenoliths from the Kaapvaal craton. Contrib. Mineral. Petrol. 174.
Rosen, O.M., Manakov, A.V., Serenko, V.P., 2005. Paleoproterozoic collisional system and diamondiferous lithospheric keel of the Yakutian kimberlite province. Russ. Geol. Geophys. 46, 1237–1251.
Rossman, G.R., Aines, D.R., 1991. The hyrdous component in garnets: Grossular-hydrogrossular. Am. Mineral. 76, 1153–1164.
Sautter, V., Harte, B., 1988. Diffusion gradients in an eclogite xenolith from the Roberts Victor kimberlite pipe; 1: mechanism and evolution of garnet exsolution in Al2O3-rich clinopyroxene. J. Petrol. 1325–1352.
Sautter, V., Harte, B., 1990. Diffusion gradients in an eclogite xenolith from the Roberts Victor kimberlite pipe: (2) kinetics and implications for petrogenesis. Contrib. Mineral. Petrol. 105, 637–649.
Skogby, H., 2006. Water in Natural Mantle Minerals I: Pyroxenes. Rev. Mineral. Geochem. 62, 155–167.
Skogby, H., Janak, M., Broska, I., 2016. Water incorporation in omphacite: concentrations and compositional relatios in ultrahigh-pressure eclogites from Phorje, Eastern Alps. Eur. J. Mineral. 28, 631–639.
Smyth, J.R., Caporuscio, F.A., McCormick, T.C., 1989. Mantle eclogites: evidence of igneous fractionation in the mantle. Earth Planet. Sci. Lett. 93, 133–141.
Sobolev, N.V.J., Kuznetsova, I.K., Zyuzin, N.I., 1968. The petrology of grospydite xenoliths from the Zagadochnaya kimberlite pipe in Yakutia. J. Petrol. 9, 253–280.
Spengler, D., Obata, M., Hirajima, T., Ottolini, L., Ohfuji, H., Tamura, A., Arai, S., 2012. Exsolution of garnet and clinopyroxene from High-Al pyroxenes in Xugou peridotite, Eastern China. J. Petrol. 53, 1477–1504.
Stalder, R., Ludwig, T., 2007. OH incorporation in synthetic diopside. Eur. J. Mineral. 19, 373–380.
Sun, J., Rudnick, R.L., Kostrovitsky, S., Kalashnikova, T., Kitajima, K., Li, R., Shu, Q., 2020. The origin of low-MgO eclogite xenoliths from Obnazhennaya kimberlite, Siberian craton. Contribut. Mineral. Petrol. 175.
Sundvall, R., Stalder, R., 2011. Water in upper mantle pyroxene megacrysts and xenocrysts: a survey study. Am. Mineral. 96, 1215–1227.
Taylor, L.A., Snyder, G.A., Keller, R., Remley, D.A., Anand, M., Wiesli, R., Valley, J., Sobolev, N.V., 2003. Petrogenesis of group A eclogites and websterites: evidence from the Obnazhennaya kimberlite, Yakutia. Contrib. Mineral. Petrol. 145, 424–443.
van Achterbergh, E., Ryan, C.G., Jackson, S.E., Griffin, W., 2001. Data reduction software for LA-ICP-MS. In: Sylvester, P. (Ed.), Laser Ablation-ICPMS in the Earth Science. Mineralogical Association of Canada, pp. 239–243.
Vitale-Brovarone, A., Alard, O., Beyssac, O., Martin, L., Picatto, M., 2014. Lawsonite metsomatism and trace element recycling in subduction zones. J. Metamorph. Geol. 32, 489–514.
Wood, B.J., Banno, S., 1973. Garnet-orthopyroxene and orthopyroxene-clinopyroxene relationships in simple and complex systems. Contrib. Mineral. Petrol. 42, 109–124.
Xia, Q.-K., Dallai, L., Deloule, E., 2004. Oxygen and hydrogen isotope heterogeneity of clinopyroxene megacrysts from Nushan Volcano, SE China. Chem. Geol. 209, 137–151.
Xu, W., Liu, X., Wang, Q., Lin, J., Wang, D., 2004. Garnet exsolution in garnet clinopyroxenite and clinopyroxenite xenoliths in early Cretaceous intrusions from the Xuzhou region, eastern China. Mineral. Mag. 68, 443–453.
Zhang, X., Ganguly, J., Ito, M., 2009. Ca-Mg diffusion in diopside: Tracer and chemical inter-diffusion coefficients. Contrib. Mineral. Petrol. 159.